Deep learning-based susceptibility assessment and prediction of landslides triggered by earthquake and rainfall using autoencoder combined with random forest

KOUNGHOON NAM

Feb. 2020

博士論文

Deep learning-based susceptibility assessment and prediction of landslides triggered by earthquake and rainfall using autoencoder combined with random forest

KOUNGHOON NAM

平成29年度入学

島根大学大学院総合理工学研究科博士後期課程

総合理工学専攻 地球科学・地球環境　コース

主指導教員: 汪 発武

令和 2 年 2 月

Abstract

Landslide affecting factors are either not correlated or non-linearly correlated. They are more complex, as well as it has the non-linear relationship between landslides and landslide affecting factors, which results in limiting the predictive performance of traditional machine learning methods for landslide susceptibility maps. In order to overcome these problems, a novel deep learning-based algorithm that combines both deep learning and machine learning is proposed for landslide susceptibility assessment and prediction. The autoencoder technique in deep learning takes advantage of dimension reduction by stacked autoencoder (StAE) and dropout by sparse autoencoder (SpAE) for non-linear correlations of the landslide affecting factors and gives better feature descriptions than the original data.

Physically-based methods, using geographic information system (GIS) and remote sensing for landslide susceptibility assessment and slope stability analysis, are more accurate than using statistical approaches, but which are not suitable for large areas. Therefore, statistical and data mining methods have received much attention. It is necessary for decision maker to recognize large areas, where landslides are expected, for land use planning and disaster control. Landslide susceptibility prediction based on statistical approaches can achieve this goal efficiently.

As a case study for landslides triggered by earthquake, Iburi region of Hokkaido in Northern Japan is selected. The aim of this study is to evaluate the performance of an autoencoder framework based on deep neural network for prediction and susceptibility assessment of regional landslides triggered by earthquakes. Thousands of landslides were triggered by the Hokkaido Eastern Iburi earthquake on 6 September 2018 in Iburi regions of Hokkaido, Northern Japan. Most of the landslides (5,627 points) occurred intensively between the epicenter and the station that recorded the highest peak ground acceleration. In Iburi region, there is a high possibility of earthquakes occurring in the future. Effective prediction and susceptibility assessment methods are required for sustainable management and disaster mitigation in the study area. By applying 12 sampling sizes and 12 landslide affecting factors, 12 landslide susceptibility maps were produced using an autoencoder framework. The results of the model were evaluated using qualitative and quantitative assessment methods. The sampling sizes on the non-landslide points randomly generated from

plain and mountain (PM) and a mountainous only zone (M) affected different prediction abilities of the model's performance. The 12 susceptibility maps, including landslide susceptibility index, indicated various spatial distributions of landslide susceptibility values in both PM and M. The highly accurate models explicitly distinguished the potential areas of landslide from stable areas without expanding the spatial extent of the potential landslide areas. The autoencoder is proved to be an effective and efficient method for extracting spatial patterns through unsupervised learning for the prediction and susceptibility assessment of landslide areas.

For case study of landslides triggered by extreme rainfall, the landslides in Oda City and Gotsu City in Shimane Prefecture, southwestern Japan are used. This study proposes the combined method of the advantage of deep learning and the benefits of machine learning for landslide susceptibility assessment. Both stacked autoencoder and sparse autoencoder in deep learning are combined with random forest acquired from results of a better predictive performance between support vector machine and random forest in machine learning. The prediction performance of random forest (RF) was evaluated better than support vector machine (SVM) in traditional machine learning so that RF was combined with both StAE and SpAE. The results show that the prediction ratio of combined classifiers was 93.2 % for StAE combined with RF model and 92.5 % for SpAE combined with RF model, which were higher than those of the SVM (87.4 %), RF (89.7 %), StAE (84.2 %), and SpAE (88.2 %), respectively. This study provides an example that combined classifiers give a better predictive ratio than a single classifier. The asymmetric and unsupervised autoencoder combined with RF can exploit optimal non-linear features from landslide affecting factors successfully, outperforms some conventional machine learning methods, and is promising for landslide susceptibility assessment and prediction.

Acknowledgement

First and foremost, I would like to express my deepest appreciation to my enthusiastic supervisor, Prof. Fawu Wang, for his continuous guidance, support, and encouragement throughout course of my doctoral degree, which incented me to widen my research from various perspectives. Especially, his immense knowledge in the area of field investigation and soil mechanics give me better understanding to address problem confronted during the research. His tremendous motivation and positive attitude towards life and research will be lifelong benefits for me.

Many thanks to Dr. Zili Dai, Mr. Prakash Dhungana, Ms. Ran Li, Mr. Yoshiharu Yokota, Mr. Akinori Iio, Ms. Rong Zhou, Dr. Shuai Zhang in Chinese Academy of Geological Sciences, and Prof. Feng Ji in Chengdu University of Technology. The life, the field works, the seminars and the conferences we shared together will be lifelong reminiscence.

My deepest gratitude also goes to Prof. Gyo-Cheol Jeong in Andong National University and Dr. Byung-Gon Chae in Korea Institute of Geoscience and Mineral Resources for their moral support. I would not have initiated and made it without their encouragement, assistance and advice to study abroad under the supervision of Prof. Fawu Wang.

<div align="right">

Kounghoon NAM

January 2020

Matsue, Japan

</div>

Table of contents

List of tables

List of figures

Introduction

1.1 Background

Landslide susceptibility assessment is a cogent research topic intended to determine the spatial probability of landslide occurrence since landslides continuously result in damages and casualties worldwide (Corominas et al. 2013). Spatial occurrence is called susceptibility, and landslide susceptibility maps generated from landslide affecting factors using statistical approaches subdivide areas into different terrains that are likely to cause certain types of landslides (Segoni et al. 2018).

Physically based methods, using geographic information system (GIS) and remote sensing for landslide susceptibility assessment, are more accurate than using statistical approaches (Alexakis et al. 2014; Ciampalini et al. 2015; Di Martire et al. 2016), which are not suitable for large areas (Tien Bui et al. 2016). Therefore, statistical and data mining methods have received much attention (Chen et al. 2018b). It is necessary for decision maker to recognize large areas, where landslides are expected, for land use planning and disaster control. Landslide susceptibility prediction based on statistical approaches can achieve this goal efficiently (Borrelli et al. 2018; Huang et al. 2019). Most of the quantitative methods for producing landslide susceptibility maps refer to regression or classification approaches between real landslide data and artificially created non-landslide data (Fell et al. 2008).

Various landslide susceptibility methods have evaluated regional landslide areas for spatial prediction and susceptibility assessment by applying different techniques, such as logistic regression (Lee S and Talib JA 2005; Ayalew and Yamagishi 2005; Bai et al. 2010; Aditian et al. 2018), naïve Bayes (Tien Bui et al. 2012; Tsangaratos and Ilia 2016), artificial neural networks (Pradhan et al. 2010; Arnone et al. 2016), support vector machines (Yao et al. 2008; Yilmaz 2010; Ballabio and Sterlacchini 2012; Xu et al. 2012), decision trees (Saito et al. 2009; Yeon et al. 2010),

and random forest (Alessandro et al. 2015; Trigila et al. 2015; Hong et al. 2016; Chen et al. 2018b; Chen et al. 2019b; Park et al. 2019) in machine learning techniques.

Recently, deep learning algorithms have made a series of revolutions in the field of classification and prediction (Huang et al. 2019) since the classification capability of a neural network to fit a decision boundary plane has become significantly more reliable (LeCun et al. 2015). These algorithms can successfully learn and extract patterns and unique features from big data (Ayinde et al. 2019). Deep learning also can effectively avoid local optimization and eliminates the need to set model parameters because of autonomous processes (Zhang et al. 2017). With the rapid development of deep neural networks, state-of-the-art learning approaches in the field of deep learning have been successfully applied in landslide susceptibility mapping and landslide deformation prediction including the following techniques: the adaptive neuro-fuzzy inference system (Park et al. 2012); recurrent neural networks (Chen et al. 2015); deep belief networks (Huang and Xiang 2018); long short-term memory (Xiao et al. 2018; Yang et al. 2019); and convolutional neural networks (Wang et al. 2019). In the field of landslide hazard assessment, unsupervised learning methods have been focused mainly on landslide inventory detection and land use classification for image analysis using interferometric synthetic-aperture radar (Mabu et al. 2019) and high-resolution satellite imaging (Liu and Wu 2016; Romero et al. 2016; Lu et al. 2019) in deep learning.

An autoencoder is a semi-unsupervised learning method with no prior knowledge, such as landslide inventory, which means that landslide and non-landslide labels and linear and non-linear correlation assumptions are not needed (Huang et al. 2019). For landslide susceptibility assessment, traditional methods for de-correlation are based on the prior assumption that there is linear correlation between landslides and non-landslides. However, landslide affecting factors are usually non-linear in practical applications. The autoencoder driven by data rather than prior knowledge can transform raw data into non-linear correlated features. The encoder and decoder are the main frameworks for unsupervised deep learning. In some techniques used in the field of deep learning, there is a lack of an encoder or a decoder. It is costly to compute an encoder and decoder to optimize algorithms for finding a code or sampling methods to achieve a framework. An autoencoder can capture both an encoder and a decoder in its structure by training landslide influencing factors (Yu and Príncipe 2019).

1.2 Objective and scope

An autoencoder modeling is a deep learning-based method. It involves a training phase with associated input and a predicting phase with target output decision values. The purpose of this study is to evaluate predictive performance of an autoencoder modeling, and the method combined with traditional machine learning for susceptibility assessment and prediction of regional landslides triggered by earthquakes in Hokkaido and extreme rainfall in Shimane Prefecture, Japan.

As a study case for landslides triggered by earthquake, Iburi region of Hokkaido in Northern Japan is selected. The aim of this study is to carry out predictive performance of earthquake-induced landslides distribution in the area affected by 2018 Hokkaido Eastern Iburi earthquake based on GIS and the autoencoder model by using different sampling size.

For landslides triggered by extreme rainfall, the landslides occurred in 2013 in Oda City and Gotsu City in Shimane Prefecture, southwestern Japan are used. This study proposes the combined method of the advantage of deep learning and the benefits of machine learning for landslide susceptibility assessment and prediction.

The major objectives of the research projective are as follows:

1. To construct spatial database of landslide inventory map and landslide affecting factors resulted from the Iburi earthquake in Hokkaido and extreme rainfall in Shimane Prefecture;
2. To analyze the general distribution trend between landslide inventory and landslide affecting factors;
3. To verify predictive performance of autoencoder framework by using different sampling size on the non-landslide points randomly generated from the combination zone including plain and mountain (PM) and a mountainous only zone (M) affected different prediction abilities of the model's performance in Hokkaido;
4. To increase predict performance by combining with deep learning and traditional machine learning in Shimane Prefecture;
5. To validate predict performance of autoencoder and its combined classifier by using the area under the curves based on confusion matrix.

1.3 Thesis structure

This thesis proposes novel deep learning algorithms, namely, both stacked autoencoder and sparse autoencoder combined with traditional machine learning, for landslide susceptibility assessment and prediction. Furthermore, this research is focused on the theme of understanding the spatial distribution and affecting factors of the landslides triggered by earthquakes and extreme rainfall as well as assessment of predictive performance of proposed methods.

Chapter 1 reviews previous research on the limitation of traditional machine learning and effectiveness of deep learning for landslide susceptibility assessment and prediction.

Chapter 2 describes the methodology of autoencoder in deep learning and machine learning as well as frequency ratio for correlation analysis to understand spatial distribution between landslide and landslide affecting factors.

Chapter 3 presents predictive performance using autoencoder to landslides triggered by 2018 earthquake in Iburi region, Hokkaido by applying different sampling sizes.

Chapter 4 analyzes the effect of autoencoder combined with traditional machine learning, and by comparing single classifier to landslides triggered by 2013 extreme rainfall in Oda City and Gotsu City, Shimane Prefecture.

Chapter 5 concludes the thesis by highlighting an effective and efficient method in proposed methods for extracting spatial patterns through unsupervised learning for the susceptibility assessment and prediction of landslide areas.

Methodology

In this chapter, autoencoder and random forest model are reviewed. It also describes how to evaluate correlation between landslides and landslide affecting factors using frequency ratio and validate predictive performance based on confusion matrix.

2.1 Autoencoder

Autoencoders are kinds of neural networks which reuse input values as target values. In other words, they aim to reconstruct input values and have direct connection with conventional neural networks. Autoencoders are a specific type of feedforward neural networks where the input is the same as the output, applying backpropagation neural networks. They compress the input into a lower-dimensional code and then reconstruct the output from this representation. In this section, it reviews deep learning techniques such as feedforward neural networks and backpropagation neural networks, and types of autoencoder including stacked autoencoder and sparse autoencoder.

2.1.1 Feedforward neural networks

A given node takes the weighted sum of its inputs and passes it through a non-linear activation function. This is the output of the node, which then becomes the input of another node in the next layer (Fig. 2.1). It has a p-dimensional input random vector X and a target random variable Y. Let $\{(x^{(1)}, y^{(1)}), (x^{(2)}, y^{(2)}), \cdots, (x^{(m)}, y^{(m)})\}$ be training sample set. The single neuron model has the form in Eq. 2.1 (Shin, 2015).

$$h_{w,b}(x) = f(\mathbf{W}^t\mathbf{x} + b) = f(\sum_{i=1}^{p} W_i x_i + b) \tag{2.1}$$

where

$$f(z) = \frac{1}{1 + e^{-z}} \tag{2.2}$$

is the sigmoid activation function as Eq. 2.2.

Feedforward neural networks consist of many neurons whose connection forms a hierarchical directed acyclic graph. The computation that the neural network represents is given by Eqs. 2.3-2.6

$$a_1^{(2)} = f(W_{11}^{(1)}x_1 + W_{12}^{(1)}x_2 + W_{13}^{(1)}x_3 + b_1^{(1)}) \tag{2.3}$$

$$a_2^{(2)} = f(W_{21}^{(1)}x_1 + W_{22}^{(1)}x_2 + W_{23}^{(1)}x_3 + b_2^{(1)}) \tag{2.4}$$

$$a_3^{(2)} = f(W_{31}^{(1)}x_1 + W_{32}^{(1)}x_2 + W_{33}^{(1)}x_3 + b_3^{(1)}) \tag{2.5}$$

$$h_{w,b}(x) = a_1^{(3)} = f(W_{11}^{(2)}a_1^{(2)} + W_{12}^{(2)}a_2^{(2)} + W_{13}^{(2)}a_3^{(2)} + b_1^{(2)}) \tag{2.6}$$

where

$a_i^{(l)}$: activation (output) of unit i in layer l

$W_{ij}^{(l)}$: weight associated with unit j in layer l and unit i in layer $l+1$

$b_i^{(l)}$: bias associated with unit i in layer $l+1$

Notation for autoencoder description is listed in Table 2.1.
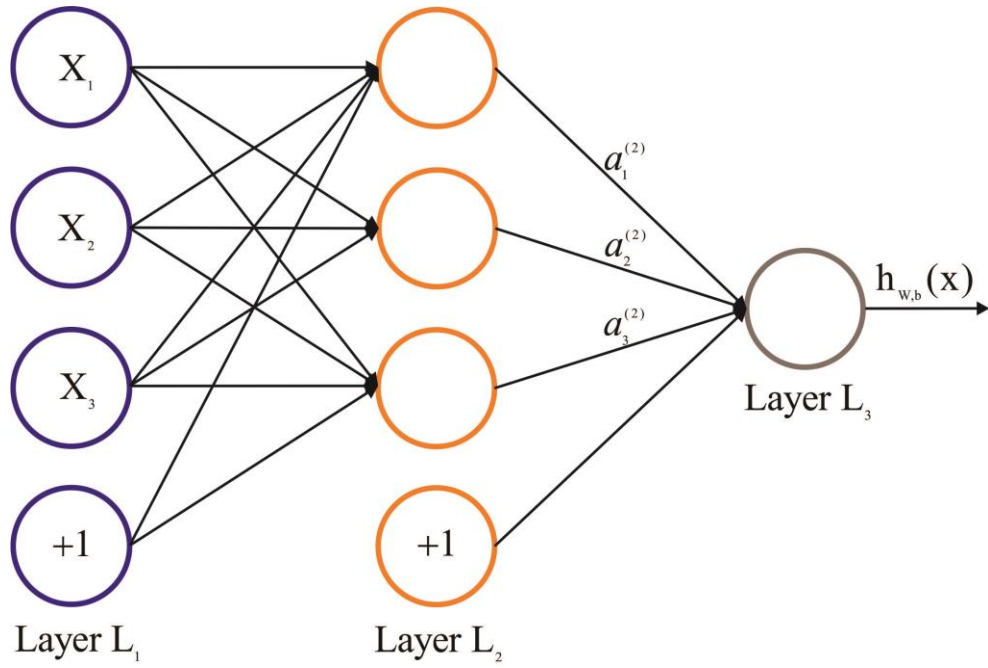
Fig. 2.1 Diagram of feedforward neural network (modified from Ng, 2011)

2.1.2 Backpropagation neural network

If it uses a fully connected neural network with n_l layers, it should estimate in Eq 2.7 and 2.8.

$$W = \{W_{ij}^{(l)} \mid l = 1, \cdots, n_l, \ i = 1, \cdots, s_{l+1}, \ j = 1, \cdots, s_l\} \tag{2.7}$$

$$b = \{b_i^{(l)} \mid l = 1, \cdots, n_l, \ i = 1, \cdots, s_{l+1}\}. \tag{2.8}$$

It can estimate network by using empirical risk minimization principle using squared-error loss function in the regression setting in Eq. 2.9.

$$(\hat{W}, \hat{b}) = \underset{W, b}{\arg\min}[\frac{1}{m}\sum_{i=1}^{m}(\frac{1}{2}\|h_{w,b}(x^{(i)}) - y^{(i)}\|^2] \tag{2.9}$$

To avoid overfitting issue, it can add a ridge type penalty term in Eq. 2.10.

$$J(W, b) = [\frac{1}{m}\sum_{i=1}^{m}(\frac{1}{2}\|h_{w,b}(x^{(i)}) - y^{(i)}\|^2] + \frac{\lambda}{2}\sum_{l=1}^{n_l-1}\sum_{i=1}^{s_l}\sum_{j=1}^{s_{l+1}}\left(W_{ji}^{(l)}\right)^2 \tag{2.10}$$

Parameters in feedforward neural networks are minimizers of target function $J(W, b)$. To minimize $J(W, b)$, gradient descent algorithm can be used.

For gradient descent algorithm, initialize (W, b), and then updates Eq. 2.11 and 2.12.

$$W_{ij}^{(l)} \leftarrow W_{ij}^{(l)} - a\frac{\partial}{\partial W_{ij}^{(l)}}J(W, b) \tag{2.11}$$

$$b_i^{(l)} \leftarrow b_i^{(l)} - a\frac{\partial}{\partial b_i^{(l)}}J(W, b) \tag{2.12}$$

where α is the learning rate.

Simple back-propagation algorithm can be used to compute derivatives as Eq. 2.13

$$\frac{\partial}{\partial W_{ij}^{(l)}} J(W, b) = \frac{\partial}{\partial W_{ij}^{(l)}} \frac{1}{2} \| h_{w,b}(x) - y \|^2 + \lambda W_{ji}^{(l)} \qquad (2.13)$$

For backpropagation algorithm (Ng, 2011), process is as follows:

(1) Performs a feed-forward pass, computing the activations for layers L_2, L_3 and so on up to the output layer L_{nl}.

(2) Set each output unit i as Eq. 2.14

$$\delta_i^{(nl)} = \frac{\partial}{\partial z_i^{(nl)}} \frac{1}{2} \| y - h_{w,b}(x) \|^2 = -(y_i - a_i^{(nl)}) \cdot f'\left(z_i^{(nl)}\right) \qquad (2.14)$$

(3) Set each node i in layer l as Eq. 2.15

$$\delta_i^{(l)} = \left(\sum_{j=1}^{s_{l+1}} W_{ji}^{(l)} \delta_i^{(l+1)}\right) f'\left(z_i^{(l)}\right) \qquad (2.15)$$

(4) Compute backpropagation algorithm in Eq. 2.16 and 2.17

$$\frac{\partial}{\partial W_{ij}^{(l)}} \frac{1}{2} \| h_{w,b}(x) - y \|^2 = a_j^{(l)} \delta_i^{(l+1)} \qquad (2.16)$$

$$\frac{\partial}{\partial W_i^{(l)}} \frac{1}{2} \| h_{w,b}(x) - y \|^2 = \delta_i^{(l+1)} \qquad (2.17)$$

The parameters of model can be estimated, combining the backpropagation and the gradient descent algorithm as Eq. 2.18.

$$(\hat{W}, \hat{b}) = \underset{W, b}{\arg\min} J(W, b) = \underset{W, b}{\arg\min} \left[\frac{1}{m} \sum_{i=1}^{m} \left(\frac{1}{2} \| h_{W,b}(x^{(i)}) - y^{(i)} \|^2\right)\right] + \frac{\lambda}{2} \sum_{l=1}^{n_l-1} \sum_{i=1}^{s_l} \sum_{j=1}^{s_{l+1}} \left(W_{ji}^{(l)}\right)^2 \qquad (2.18)$$

2.1.3 Stacked autoencoder

A stacked autoencoder (StAE) is a stacked version of autoencoders, usually consisting of 2-4 autoencoders. Rigorously, stacked autoencoders are unsupervised learning algorithm whose aim is also to reconstruct input values (Shin, 2015). The StAE is an artificial neural network, which is a special type of multi-layer perceptron. It is a type of unsupervised learning algorithm that has an asymmetric structure, in which the middle layer represents the encoding of the input data in the bottleneck layer (Yu and Príncipe 2019). The bottleneck constrains the amount of information that can traverse the full network, forcing the learned compression of the input data. The StAE is trained to reconstruct input of landslide affecting factors onto the output layer for feature representation, which prevents the simple copying of the data and the network. The middle layer has a lower dimension, employing a lower dimension that learns a nonlinear dimensionality reduction (Hinton and Salakhutdinov 2006; Charte et al. 2018) by taking advantage of the nonlinear dimensionality reduction ability. In this study, the StAE combined with back propagation neural network was processed for a lower dimension of features than the input data, which can be used for learning the most important features of the data.

2.1.4 Sparse autoencoder

The sparse autoencoder (SpAE) is the first kind of overcomplete autoencoders obtained by imposing sparsity constraints on the hidden units (Ng, 2011). Undercomplete representation autoencoders could fail to capture complex high-dimensional features of input images. To overcome it, several kinds of overcomplete autoencoders have been devised since the 2000s. It attempts to make the average of activations (outputs) of hidden units to be close to zero. The SpAE consists of an input layer, hidden layers, and an output layer. Each layer in this neural network contains a sufficient number of neurons. Dropout can randomly classify the weight of some implicit layer nodes and reduce the mutual dependence between nodes to realize the normalization of neural networks. Additionally, dropout can effectively prevent overfitting and gradient disappearance (Huang et al. 2019). The process of SpAE is as follows. First, some of the neurons in the network are randomly dropped in the mini-batch training samples and the remaining neurons are fed to the next layer. Then, after obtaining this mini-batch training sample, the deleted neurons are recovered and some neurons in the network are randomly deleted once again. The corresponding parameters are updated based on the stochastic gradient descent method, performed on the neurons that have not been removed.

More precisely, let $a_j^{(2)}(x)$ denotes the activation of j-th hidden unit corresponding to an input value x. Define the average activation of hidden unit j as Eq. 2.19

$$\hat{\rho}_j = \frac{1}{m} \sum_{i=1}^{m} \left[a_j^{(2)} \left(\mathbf{x}^{(i)} \right) \right] \tag{2.19}$$

To achieve constraint for sparsity parameter $\rho \approx 0$, it adds an additional penalty term to $J(\mathrm{W}, \mathrm{b})$ in Eq. 2.20 and 2.21

$$J_{sparse}(\mathrm{W}, \mathrm{b}) = J(\mathrm{W}, \mathrm{b}) + \beta \sum_{j=1}^{s_2} KL\left(\rho \| \hat{\rho}_j \right) \tag{2.20}$$

$$KL\left(\rho \| \hat{\rho}_j \right) = \rho \log \frac{\rho}{\rho_j} + (1 - \rho) \log \frac{1-\rho}{1-\rho_j} \tag{2.21}$$

Note that $KL\left(\rho\|\hat{\rho}_j\right)$ is the Kulback-Leiber divergence between Ber (ρ) and Ber ($\hat{\rho}_j$). To estimate the sparse autoencoder, it can use the modified version of the back-propagation algorithm to compute derivative of $J_{sparse}(W, b)$.

For backpropagation of sparse autoencoder,

(1) Perform a feed-forward pass, computing the activations for the hidden layer L_2 up to the output layer L_3.

(2) For each output unit i, set as Eq. 2.22

$$\delta_i^{(3)} = \frac{\partial}{\partial z_i^{(3)}} \frac{1}{2} \| x - h_{w,b}(x) \|^2 = -(x_i - a_i^{(3)}) \cdot f'\left(z_i^{(3)}\right) \tag{2.22}$$

(3) For each node i in the hidden layer, set as Eq. 2.23

$$\delta_i^{(2)} = \left(\left(\sum_{j=1}^{s_2} W_{ji}^{(2)}\delta_i^{(3)}\right) + \beta\left(-\frac{\rho}{\hat{\rho}_i} + \frac{1-\rho}{1-\hat{\rho}_i}\right)\right) f'(z_i^2) \tag{2.23}$$

(4) Compute in Eq. 2.24 and 2.25

$$\frac{\partial}{\partial W_{ij}^{(2)}} \frac{1}{2} \| h_{w,b}(x) - x \|^2 = a_j^{(2)}\delta_i^{(3)} \tag{2.24}$$

$$\frac{\partial}{\partial b_i^{(2)}} \frac{1}{2} \| h_{w,b}(x) - x \|^2 = \delta_i^{(3)} \tag{2.25}$$

It can estimate the parameters of the sparse autoencoder, combining the above backpropagation and the gradient descent algorithm in Eq. 2.26

$$(\hat{W},\hat{b}) = \arg\min_{W, b} J_{sparse}(W, b) = J(W, b) + \beta\sum_{j=1}^{s_2} KL\left(\rho\|\hat{\rho}_j\right) \tag{2.26}$$

Table 2.1 Notation for autoencoder description (modified from Ng, 2011)

x	Input features for a training example, $x \in \mathbb{R}^n$.
y	Output or target values. Here, y can be vector valued. In the case of an autoencoder, $y = x$.
$(x^{(i)}, y^{(i)})$	The i-th training example
$h_{W,b}(x)$	Output of hypothesis on input x, using parameters W, b. This should be a vector of the same dimension as the target value y.
$W_{ij}^{(l)}$	The parameter associated with the connection between unit j in layer l, and unit i in layer $l+1$.
$b_i^{(l)}$	The bias term associated with unit i in layer $l+1$. Can also be thought of as the parameter associated with the connection between the bias unit in layer l and unit i in layer $l+1$.
θ	Parameter vector. It is useful to think of this as the result of taking the parameters W, b and unrolling them into a long column vector.
$a_i^{(l)}$	Activation (output) of unit i in layer l of the network. In addition, since layer L_1 is the input layer, it also has $a_i^{(l)} = x_i$.
$f(\cdot)$	The activation function. Throughout these notes, it used $f(z) = \tanh(z)$.
$z_i^{(l)}$	Total weighted sum of inputs to unit i in layer l. Thus, $a_i^{(l)} = f(z_i^{(l)})$
α	Learning rate parameter
s_l	Number of units in layer l (not counting the bias unit)
n_l	Number layers in the network. Layer L_1 is usually the input layer and layer L_{nl} the output layer.
λ	Weight decay parameter
$\hat{x}$	For an autoencoder, its output; i.e., its reconstruction of the input x. Same meaning as $h_{W,b}(x)$.
ρ	Sparsity parameter, which specifies desired level of sparsity
$\hat{\rho}_i$	The average activation of hidden unit i in the sparse autoencoder
β	Weight of the sparsity penalty term (in the sparse autoencoder objective)

2.2 Random forest

The random forest, as a classification tree algorithm, with repeated dichotomy data can significantly reduce the computations required for classification and regression. In RF algorithms, predictive models are established by utilizing many decision trees. Based on randomly selected variables and samples, these trees and their decisions are generated. Once the model is established, the samples are first sorted individually according to all decision trees in the model, and then by all trees (Huang and Zhao, 2018). The proportion of decision tree estimates and generates landslide susceptibility indexes, which can predict landslide occurrence between all decision tree in RF model (Goetz et al. 2015).

A random forest is a predictor consisting of a collection of M randomized regression trees. For the j-th tree in the family, the predicted value at the query point x is denoted by $m_n(\mathrm{x}; \Theta_j, D_n)$, where $\Theta_1, \cdots, \Theta_m$ are independent random variables, distributed the same as a generic random variable Θ and independent of D_n. The variable Θ is used to resample the training set prior to the growing of individual trees and to select the successive directions for splitting more precise definitions will be given later (Scornet, 2015). The trees are combined to form the (finite) forest estimate in Eq 2.27:

$$m_{M,n}(\mathrm{x}; \Theta_1, \cdots, \Theta_m, D_n) = \frac{1}{M} \sum_{j=1}^{M} m_n(\mathrm{x}; \Theta_j, D_n) \tag{2.27}$$

Since M may be chosen arbitrarily large, limited only by available computing resources, and consider instead of the infinite forest estimate in Eq. 2.28:

$$m_{\infty,n}(\mathrm{x}; D_n) = \mathrm{E}_\Theta \left[m_n(\mathrm{x}; \Theta_j, D_n) \right] \tag{2.28}$$

In this definition, E_Θ denotes the expectation with respect to the random parameter Θ, conditional on D_n. The operation $M \to \infty$ is justified by the law of large numbers using Eq. 2.29, which asserts that almost surely, conditional on D_n,

$$\lim_{M \to \infty} m_{M,n}(\mathrm{x}; \Theta_1, \cdots, \Theta_m, D_n) = m_{\infty,n}(\mathrm{x}; D_n) \tag{2.29}$$

For classification, the binary supervised classification problem, the random response Y takes values in {0, 1} and, given X, one has to guess the value of Y. A classifier or classification rule m_n is consistent as Eq. 2.30

if its conditional probability of error

$$L(m_n) = P[m_n(X) \neq Y \mid D_n]$$ (2.30)

satisfies in Eq. 2.31

$$\lim_{n \to \infty} EL(m_n) = L^*$$ (2.31)

where L^* is the error of the optimal *Bayes* classifier in Eq. 2.32

$$m^*(x) = \begin{cases} 1 & \text{if } P[Y=1|X=x] > P[Y=0|X=x] \\ 0 & \text{otherwise.} \end{cases}$$ (2.32)

In the classification situation, the random forest classifier is obtained using Eq 2.33 via a majority vote among the classification trees,

$$m_{M,n}(x; \Theta_1, \cdots, \Theta_m, D_n) = \begin{cases} 1 & \text{if } \dfrac{1}{M} \sum_{j=1}^{M} m_n(x; \Theta_j, D_n) > 1/2 \\ 0 & \text{otherwise.} \end{cases}$$ (2.33)

2.3 Frequency ratio for correlation analysis

The assumption of conditions that are similar to the past is very important for landslide susceptibility mapping (Lee and Talib 2005). Probabilistic (statistical) approaches are based on relationships between each landslide affecting factor and the distribution of past landslides (Lee and Talib 2005) and this relationship can be evaluated quantitatively using the frequency ratio model. The number of landslide pixel grid in each class is evaluated and the frequency ratio for each factor class is assigned by dividing the landslide ratio by the area ratio. The frequency ratio shows the correlation between landslides and affecting factors in a specific area. If this ratio is greater than 1, then the relationship between a landslide and the affecting factor's class will be strong but if the ratio is less than 1, then the relationship will be weak and if the value is 1, it means an average correlation (Meten et al. 2015). The spatial relationship between the landslide location and each landslide factor was analyzed and the ratings for each factor's class were assigned to each class in a specific factor. Then the frequency ratio ratings of factors in the form of raster maps were summed to form the landslide susceptibility index (*LSI*) using Eq. 2.34

$$LSI = \sum_{i=1}^{n} Fr \qquad (2.34)$$

Where *Fr* is the raster map of each landslide affecting factor in which the frequency ratio values are assigned to it. The current study tries to analyze the effect of different combinations of landslide factors on the performance of the frequency ratio model in order to get the minimum number of landslide factors which can produce a susceptibility map with higher prediction accuracy similar to combining many landslide factors using the mathematical combination theory.

2.4 Confusion matrix for validation of predictive performance

Several commonly used classification performances were measured based on the confusion matrix (Table 2.2 and Fig. 2.2), which is employed to evaluate model predictive performance. Each grid cell of the landslide susceptibility map had a unique value representing the landslide susceptibility value. All grid cells were determined as one of four elements: true positive (TP), true negative (TN), false positive (FP), and false negative (FN). Precision gives the percentage of true positives as a ratio over all cases that should have been true in Eq. 2.35. Recall or the true positive rate (TPR) measures the number of cases that were predicted as positive that should indeed be positive in Eq. 2.36. The true negative rate (TNR) measures the proportion of actual negatives that are correctly identified in Eq. 2.37. The false positive rate (FPR) is calculated as the ratio between the number of negative events wrongly categorized as positive (false positives) and the total number of actual negative events in Eq. 2.38. Accuracy is the overall percentage of samples that are correctly predicted as defined in Eq. 2.39.

$$\text{Precision} = \frac{TP}{TP + FP} \tag{2.35}$$

$$\text{Recall } (TPR \text{ or } sensitivity) = \frac{TP}{TP + FN} \tag{2.36}$$

$$\text{TNR } (specificity) = \frac{TN}{TN + FP} \tag{2.37}$$

$$\text{FPR } (1 - specificity) = \frac{FP}{FP + TN} \tag{2.38}$$

$$\text{Accuracy} = \frac{TP + TN}{TP + FP + TN + FN} \tag{2.39}$$

The precision and recall curve present the relationship between correct landslide predictions and the proportion of landslides detected. The TPR (sensitivity) and TNR (specificity) curve indicates the relationship between the correctly identified classes in both labels.

Table 2.2 Statistical indexes for model evaluation

Condition	Description	Evaluation
TP (True Positive)	The number of samples that have been predicted **correctly** as **landslides**.	To evaluate the prediction performance of the model for **landslides**
FN (False Negative)	The number of samples that have been predicted **incorrectly** as **landslides**.	
TN (True Negative)	The number of samples that have been predicted **correctly** as **non-landslides**.	To evaluate the prediction performance of the model for **non-landslides**
FP (False Positive)	The number of samples that have been predicted **incorrectly** as **non-landslides**.	
TPR (True Positive Rate)	The true positive rate (TPR) is defined as the ratio of **true positive** to the sum of **true positive** and **false negative** to the number of validation samples.	To evaluate the **predictive ratio** for landslide susceptibility assessment and prediction (see **Chapter 3 and 4**)
FPR (False Positive Rate)	The false positive rate (FPR) is defined as the ratio of **false positive** to the sum of **false positive** and **true negative** to the number of validation samples	
Accuracy	Accuracy is the overall percentage of samples that are correctly predicted.	If the data set is **unbalanced**, accuracy is not a reliable metric for the real performance of a classifier, because it will yield misleading results (see **Chapter 3**).

		True landslides		
		Landslides (Ls)	Non-Ls	
Predicted landslides	Landslides	TP (True Positive)	FP (False Positive)	Accuracy $= \dfrac{TP+TN}{TP+FP+TN+FN}$
	Non-Ls	FN (False Negative)	TN (True Negative)	Precision $= \dfrac{TP}{TP+FP}$
		TPR (True Positive Rate) $= \dfrac{TP}{TP+FN}$	FPR (False Positive Rate) $= \dfrac{FP}{FP+TN}$	TNR (True Negative Rate) $= \dfrac{TN}{TN+FP}$

Fig. 2.2 Confusion matrix for validation of landslide susceptibility assessment

Landslides triggered by 2018 Iburi earthquake

in Hokkaido

In this chapter, the predictive performance of an autoencoder framework is evaluated for susceptibility assessment and prediction of landslides triggered by the 2018 Hokkaido Eastern Iburi earthquake. By applying 12 sampling sizes and 12 landslide affecting factors, 12 landslide susceptibility maps are produced using an autoencoder modeling. The autoencoder is proved to be an effective and efficient method with more than 89% of predictive performance on 12 models.

3.1 Study area

The study area was located in tectonically active regions between the Pacific, North American, Eurasian, and Philippine plates, where exist the deepest trenches, such as the Northeast Honshu Arc-Japan Trench and the Kuril Arc-Trench in Fig. 3.1 (Kimura 1994; Tamaki et al. 2010). These trenches are mainly composed of sedimentary Quaternary deposits and Neogene rocks, and the soil layers consist of pyroclastic tephra deposits mainly derived from Tarumae volcano, including pumice, volcanic ash, and clay, which were found distributed over a wide area (Tajika et al. 2016). The Hidaka mountains collision between the NE Japan and Kuril arcs as well as fluids from dehydration of the subducting Pacific plate caused this big event and its unusual focal depth. Similar attenuation structures are revealed in source zones of the 1970 Hidaka earthquake (Mj 6.7) and the 1982 Urakawa-oki earthquake (Mj 7.1) in Fig. 3.2 (Hua et al. 2019). The 2018 Eastern Iburi earthquake with a focal depth of ~37 km is quite unusual because it is much deeper than other inland crustal events in the region, and it seems located in the uppermost mantle, considering the Moho depth of ~33 km in the source area. The surface area of the distorted portion tends to increase as the slab subducts, and thus many fractures are considered to have progressively developed in the slab during subduction. Kuritani and Nakagawa, 2016 suggests that the intense dehydration of

the slab was caused by the injection of the higher-temperature materials into the slab. During the subduction of the Pacific plate, the distorted portion of the slab was progressively fractured, and hot mantle materials were injected locally into the relatively large-scale fracture from underneath the slab (Fig. 3.3). The geology units in the study area were divided into sixteen classes incorporating water, and only nine classes were observed to be related to landslide occurrence (Fig. 3.4). For intensive landslides in ellipse area, the majority of landslides occurred in geology is Miocene non-marine sediments from Hidaka mountains collisions (Fig. 3.4). The total thickness of the pyroclastic tephra deposits is about 4 - 5 m in and around the epicentral area. The highest elevation is less than 700 m. The elevation of the terrain that was affected the most ranges from 100–200 m, with slope gradients of 25 - 30°. After a powerful typhoon (No 21, "Jebi"), the Iburi earthquake occurred. However, some reports claimed that typhoons did not pass directly through the landslide areas and that the average cumulative rain was significantly lower than in the month before the earthquake (Zhang et al. 2019). Based on the field reconnaissance, the Iburi landslides are chiefly shallow translational landslides with planar slip surfaces. Most landslides are characterized by high mobility and long run-out distance, and almost all the upper slip surfaces are exposed without overlapping of sliding mass. The shallow landslide integrated sliding body began from the collapse of the gully head, incorporated a vast sliding mass along the valley, heaped irregularly at the gully mouth, and ruined several houses and drainage system (Fig. 3.5 a, b, c, d). Figure 3.5 e and f illustrate the soil composition of the landslide in the right flank and in the scarp integrated sliding body. The left-hand side of the scarp, which is located near the ridge of the hill slope and did not collapse due to its shallower dip angle, exhibits a stratigraphic sequence of pyroclastic deposits originating from the Tarumai Volcano. Isopach contour map and field investigation show that Ta-b (AD 1667), Ta-c (ca. 2.5 ka), and Ta-d (ca. 9 ka), with two layers of interbedded Andosols, indicating that this material corresponds to the pale-brown, clay-rich deposit found on the scarp (Fig. 3.5). The thicknesses of Ta-d, En-a and Spfa-1 pyroclastic fall deposits are 0.3~1.0 m, 0.1~1.0 m and 3~4 m respectively. The top layer has a gray-colored fine humic surface with a depth of about 300 mm. The middle layer is composed of middle humus and Tarumae-c pyroclastic fall deposits formed about 2000 years ago, while the bottom layer is composed of brownish and grayish pumice. The grain size of the bottom layer decreases from the lower to upper part. The potential sliding surface is located in the grayish-green dense pumice deposited about 9000 years ago in isopach map of pyroclastic deposits (Fig. 3.5). The soil

composition is closely related to the historic eruption and repose of the Tarumae Volcano (Tajika et al. 2016), and most coseismic landslides occurred in the interface between Ta-d pumice layers and the underlying paleosol. It is discovered through the field reconnaissance that the sliding mass moved along the planar interface of the Ta-d pumice and the underlying paleosol. Sliding zone liquefaction and grain crushing occurred within the saturated pumice layers during the down-slope motion. The pumice layers were crushed and the thickness was attenuated, which was confirmed by the clear crushed pumice strips during the field work. The crushed and liquified pumice layers spread in the deposition area and resulted in the extension of the upper sliding mass in horizontal directions. The slope angle after failure remains unchanged as the pyroclastic fall deposits were evenly deposited on the original slope surface. A sharp-free face appears at the scarp and creates a high possibility of retrogressive slope failure due to future seismic oscillation. The absence of volcanic deposits older than the Ta-d layer suggests that the last landslide in this area occurred before the eruption of Ta-d (Kameda et al. 2019). According to Kameda et al. 2019, the clay-rich Ta-d layer including halloysite-bearing soils acted as the sole weak and slippery plane within the volcanic deposits covering the slopes (Fig 3.6). The liquefaction and fluidization of this specific horizon provided the prerequisite conditions for the seismic triggering of the recent landslides.
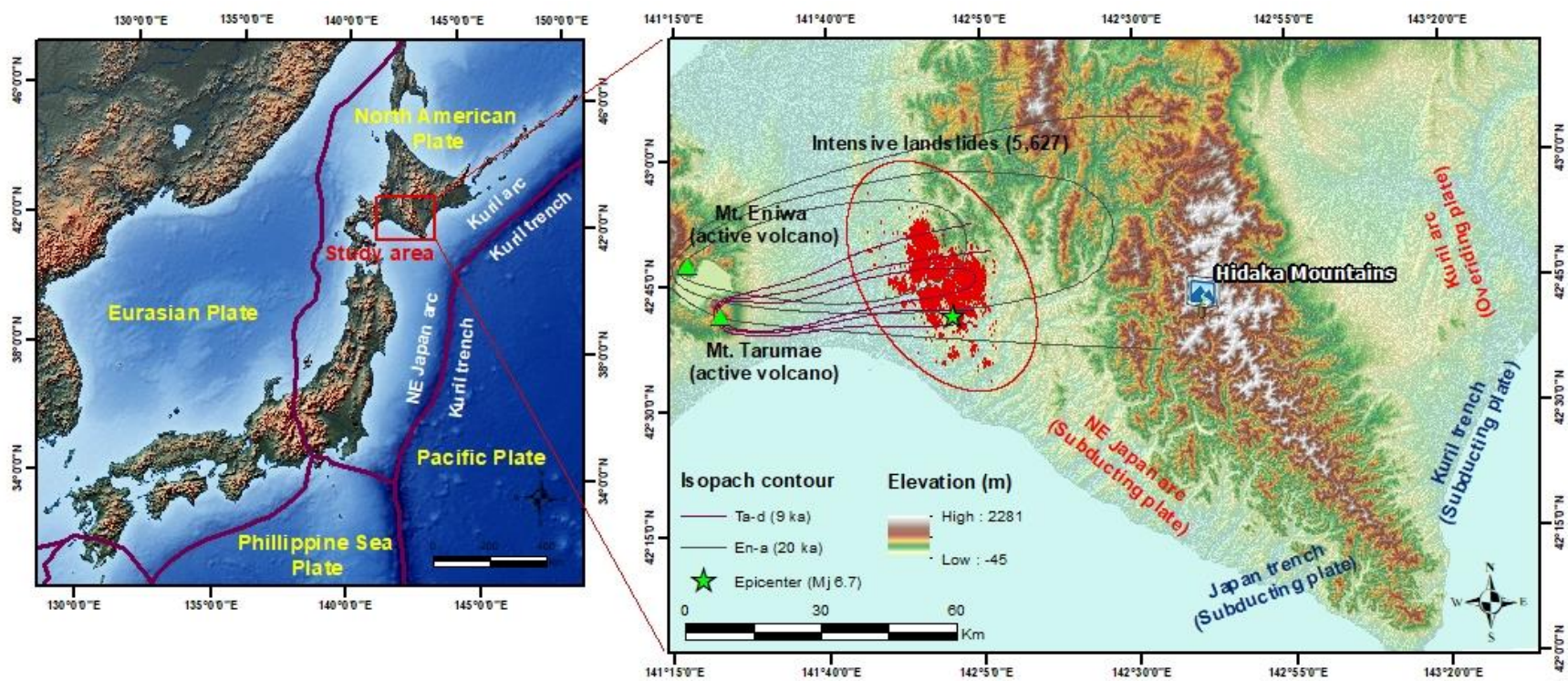
Fig. 3.1 Study area and coseismic landslide inventory map
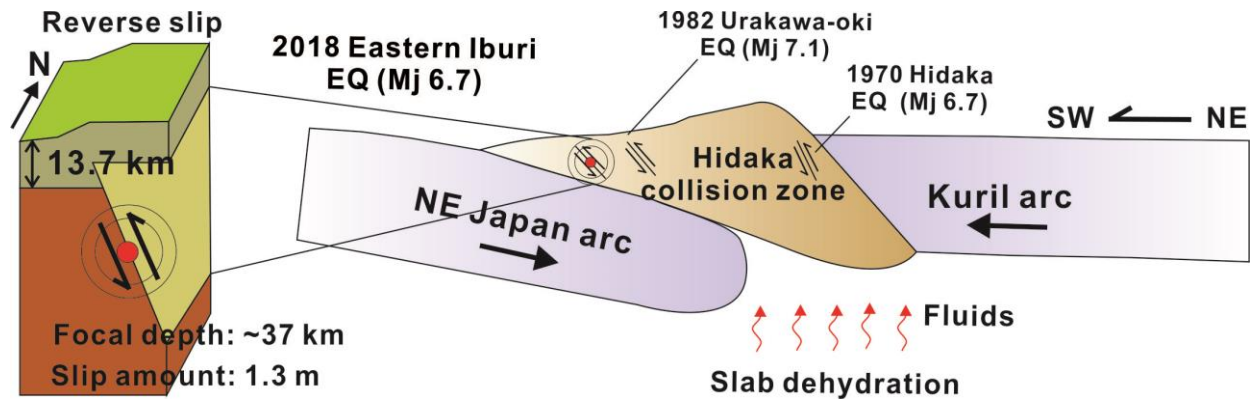
Fig. 3.2 A schematic diagram for arc-arc collision and mechanism of the three large earthquakes in the Hidaka collision zone (modified from Hua et al. 2019)
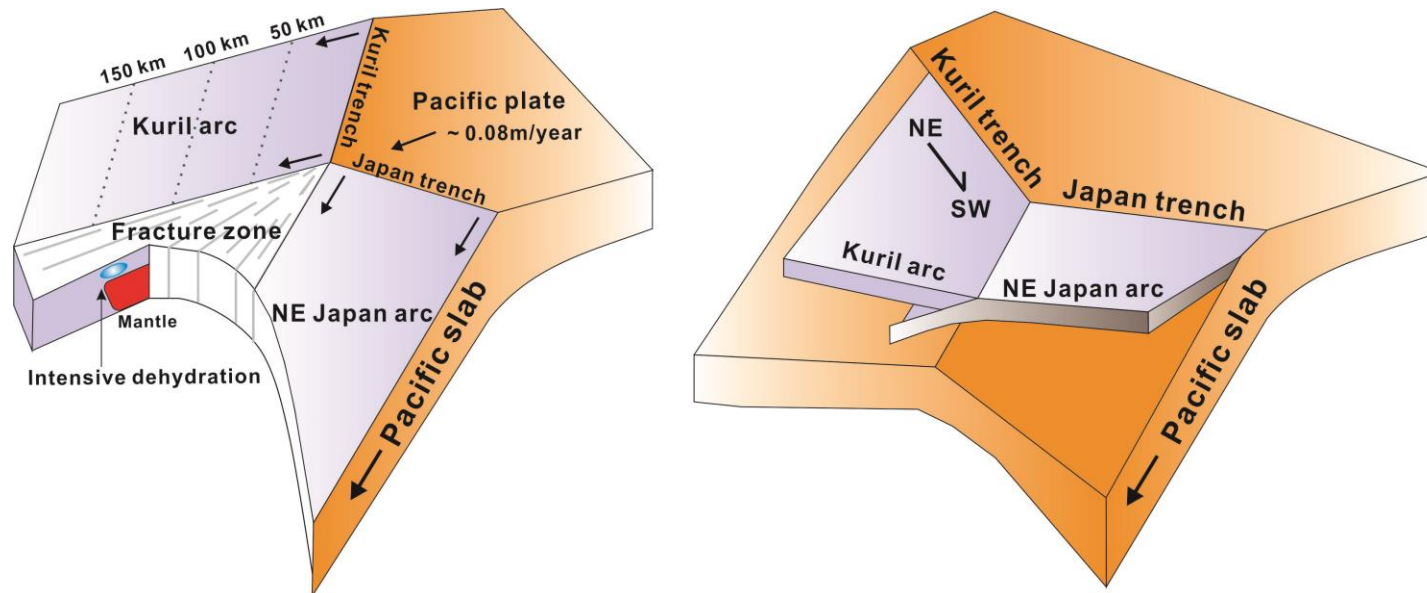
Fig. 3.3 Fracture mechanism from Kuril Arc–NE Japan Arc junction and subducting Pacific slab (modified from Kuritani and Nakagawa, 2016; Hua et al. 2019)
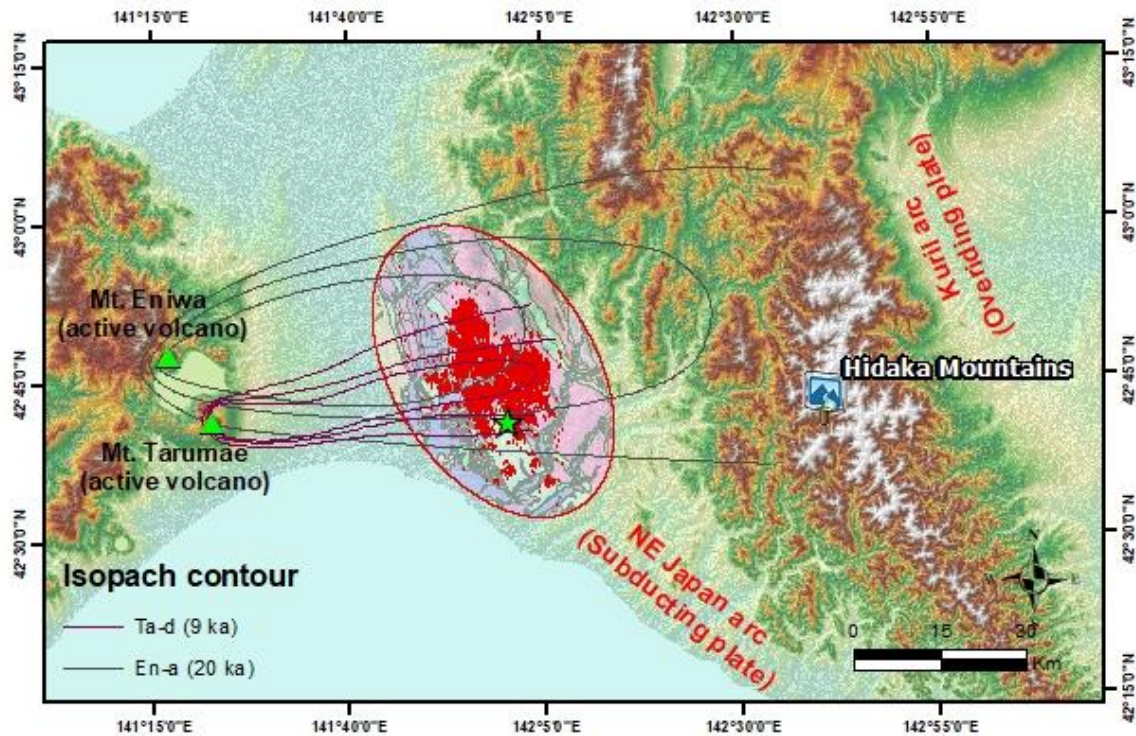
Geology

(code, description, landslides)

- Hsr, Late Pleistocene to Holocene marine and non-marine sediments (84)
- Hsw, Late Pleistocene to Holocene swamp deposits
- K2sm, Late Cretaceous marine sedimentary rocks
- N1ga, Early to Middle Miocene mafic plutonic rocks
- N1sr, Early Miocene to Middle Miocene marine and non-marine sediments (19)
- N2sn, Middle to Late Miocene non-marine sediments (4928)
- N3sn, Late Miocene to Pliocene non-marine sediments (519)
- PG2sr, Middle Eocene marine and non-marine sediments
- PG3sr, Late Eocene to Early Olligocene marine and non-marine sediments (3)
- Q2sr, Middle Pleistocene marine and non-marine sediments (22)
- Q2th, Middle Pleistocene higher terrace (39)
- Q3-Hvp, Late Pleistocene to Holocene non-alkaline pyroclastic flow volcanic rocks
- Q3sr, Late Pleistocene marine and non-marine sediments
- Q3tl, Late Pleistocene lower terrace (10)
- Uu, ultramafic rocks
- wt, water (2)

Fig. 3.4 Classification of simplified geological map (1:200,000) and coseismic landslides occurred in each unit
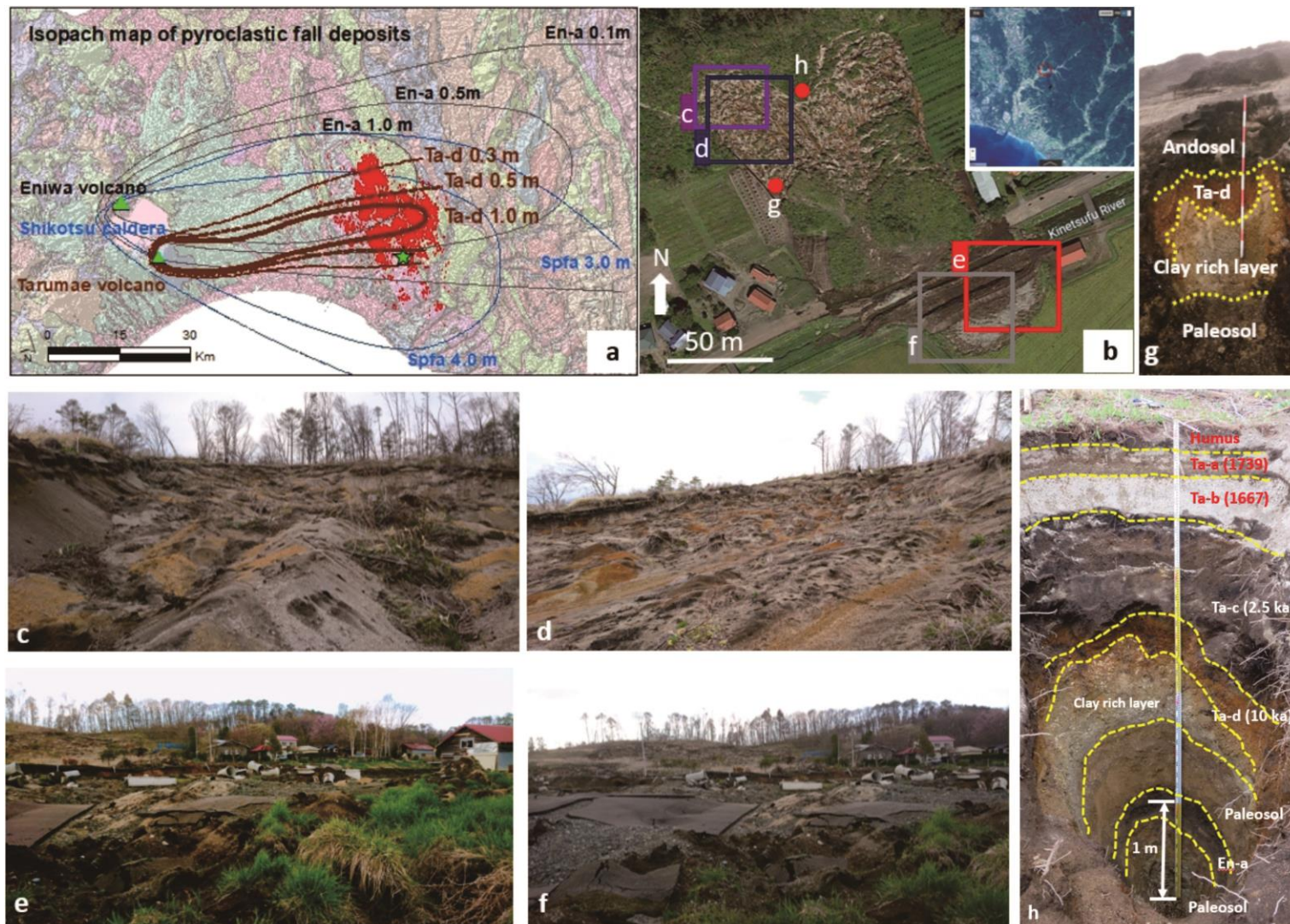
Fig. 3.5 Isopach map of pyroclastic fall deposits (Ta-a, Ta-b, Ta-c, Ta-d, En-a and Spfa-1) and field investigation on sliding surface (general view: a~d, and soil profiling e and f)
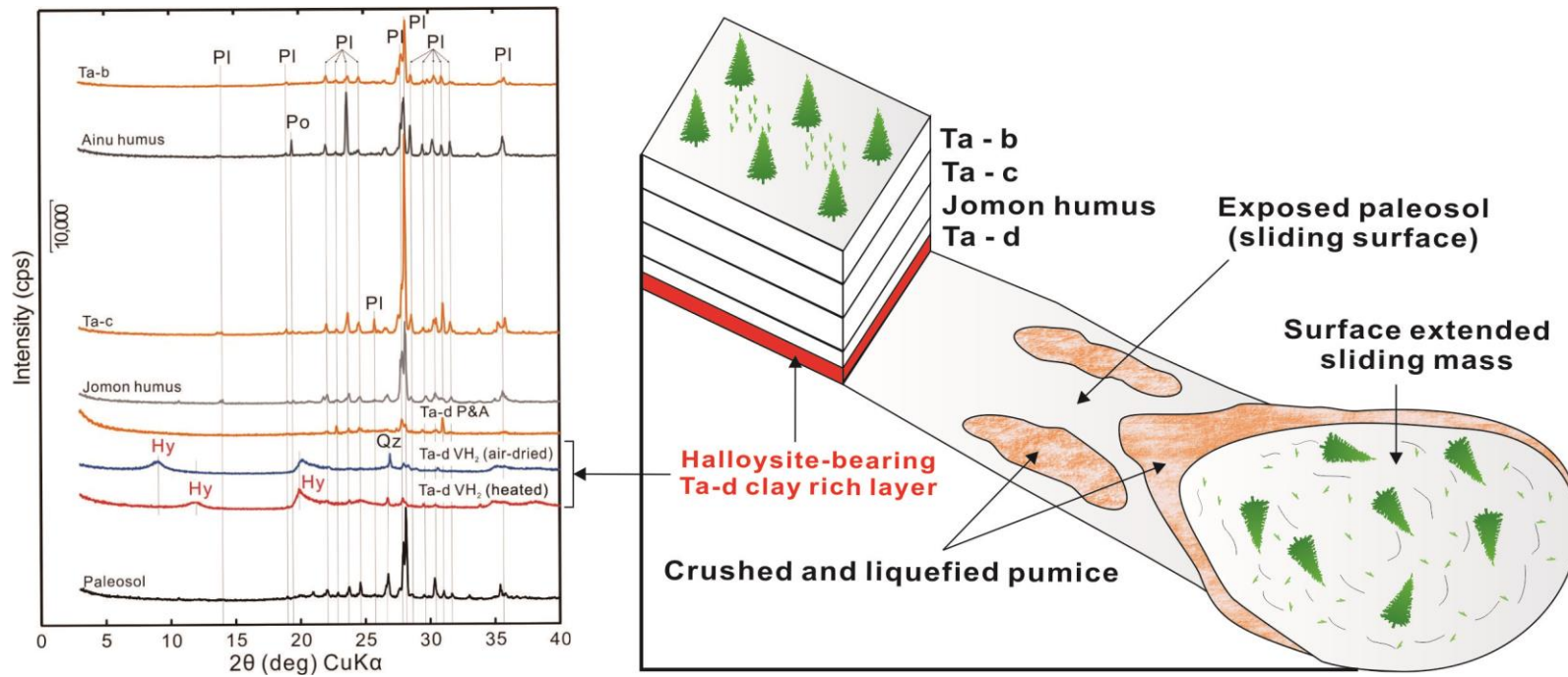
Fig. 3.6 Schematic cross-section of pyroclastic fall deposits in study area based on XRD patterns for air-dried (blue lines) and heated (red lines) samples. Hy = halloysite, Qz = quartz, Pl = plagioclase, Po = portlandite (cross section modified from Zhang et al. 2019)

3.1.1 Landslide inventory and spatial database

Aerial photographs (ortho-photographs) of the entire area affected by the earthquake were quickly taken by the Geographical Survey Institute, Japan (GSI) as well as several aerial surveying companies. The photographs were posted with analyzed satellite images on the Web as public information. The original polygon shape of 3,307 landslide sites was released by the GSI several days after the main shock (Fujiwara et al. 2019). Further reconstruction was carried out to remodify the landslide polygon based on valley lines, ridgelines, hill shade, slope, and aspect, which was generated by a resolution of 10 m. Finally, a detailed landslide inventory map incorporating 5,627 points of individual landslides was created by extracting the centroids of the landslide polygons (Fig. 3.7). This technique has been widely adopted in many landslide susceptibility methods because it is efficient in simplifying landslide data (Tsangaratos et al. 2017). There is no guiding principle for selecting the boundaries of study areas. According to Zhang et al. (2019), the directional distribution tool (Standard Deviational Ellipse) in ArcGIS 10.6 indicates ellipses containing certain percentages of the features through standard deviations in the landslide areas. The tool could be useful to guide the deployment of disaster relief operations and mitigation strategies. In the present study, to select the boundaries of the study area, an ellipse corresponding to standard deviations was generated by the directional distribution tool to indicate the general trend of the features. The tool may also be useful in the field of landslide susceptibility mapping for designating the boundaries of the study area, especially the area of landslides triggered by an earthquake as well as active faults in and around the epicenter. The sampling process is the key step in constructing landslide (events) and non-landslide points (non-events) for the database used in landslide susceptibility mapping. Several sampling strategies, such as extracting from seed cell (or gridded) points around a polygon of the landslide area (Meusburger and Alewell 2009; Van Den Eeckhaut et al. 2010) and increasing the number of non-events in the non-landslide area (King and Zeng 2001; Raja et al. 2017), have been proposed to improve model's performance, predictive capability, and reduction of statistical errors. According to King and Zeng (2001), the non-event sample size must not be large but should be two to five times greater than the events because of the disproportionate cost and effort in acquiring data on many variables, and observations that are not related to the target phenomenon (Heckmann et al. 2014). These studies were conducted mainly to evaluate logistic regression (LR) and rare events LR susceptibility models. Melchiorre et al. (2008) states that un-labeled data sets with a small number of positive examples (events) and

a large number of negative examples (non-events) negatively affect the discrimination capabilities of the trained classifier. In this study, to address these issues, 12 different sampling sizes were selected in both the PM and M. Landslide points (event points, 1) and non-landslide points (non-event points, 0) were classified and assigned ratios of approximately 1 : 1 (5627 : 5627), 1 : 2 (5627 : 11254), 1 : 3 (5627 : 16881), 1 : 4 (5627 : 22508), 1 : 5 (5627 : 28135), and 1 : 10 (5627 : 56270) in both areas. The dataset was divided into two separate training sets for unsupervised and supervised learning and one independent test set for the final model comparison. Forty percent of the landslide and non-landslide points were used as training samples for unsupervised learning. The remaining 60% were randomly selected and then used as an independent data set for supervised learning (40%) and for testing the predictive potential (20%) of the autoencoder model to check the performance of the pre-trained model.
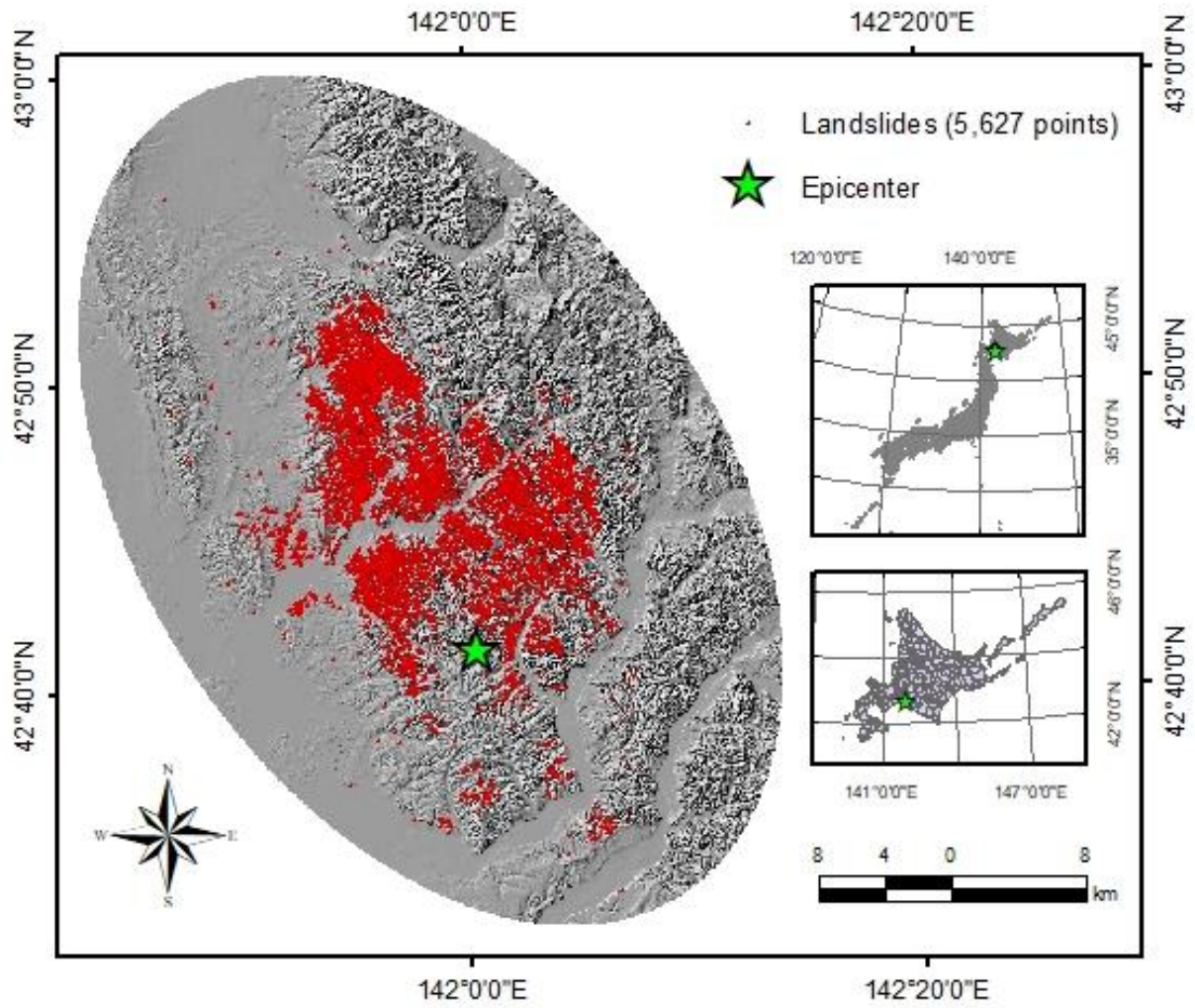
Fig. 3.7 Ellipse area of coseismic landslide for statistical analysis (modified from Zhang et al. 2019)

3.1.2 Landslide affecting factors in Hokkaido

The pixel size of the factors that influenced the landslides was set to 10 m×10 m regardless of the resolution of the original data source (Zhu et al. 2018). In landslide susceptibility modeling, a landslide may reoccur under conditions similar to past landslides (Westen et al. 2003; Lee and Talib, 2005; Dagdelenler et al. 2016). There is no common guideline for selecting the factors that influence landslides (Ayalew and Yamagishi. 2005; Yalcin 2008) In this study, 12 factors were selected to evaluate landslide susceptibility: elevation, slope angle, the normalized difference vegetation index (NDVI), distance to stream, stream density, plan curvature, profile curvature, lithology of geology, age of geology, distance to faults, distance to epicenter, and peak ground acceleration (PGA). Elevation and slope angle are key factors that have been widely employed in landslide susceptibility modeling (Colkesen et al. 2016; Althuwaynee et al. 2016). The elevation values in the study area were divided into equal intervals of 100 m: 0–100 m, 100–200 m, 200–300 m, 300–400 m, 400–500 m, and more than 500 m (Fig. 3.8 - a) The slope angle values were extracted from the DEM and classified into six groups at intervals of 10°: 0–10°, 10–20°, 20–30°, 30–40°, 40–50°, and 50–60° (Fig. 3.8 - b). The NDVI was used to qualitatively evaluate the conditions of vegetation coverage on slope surfaces, which were calculated from the near-infrared and the red band of Landsat 8 OLI (Chen et al. 2019a). The NDVI values were arranged into five classes: (-0.141)–(0.191), 0.191–0.268, 0.268–0.325, 0.325–0 388, and 0.388–0.584 (Fig. 3.8 - c). The distance to stream and stream density were evaluated as the role of the runoff and the influence on the slope erosion process by streams in landslides. Previous studies showed that the distance to stream is an important factor that controls landslide occurrence (Devkota et al. 2013; Guo et al. 2015). The distance to stream (Metan et al. 2015) was calculated for each pixel. The streams were classified as follows: 0–100 m, 100–200 m, 200–300 m, 300–400 m, and more than 400 m (Fig. 3.8 - d). The stream density was determined from the terrain hydrographic network: 0–1 $\mathbf{m^{-1}}$, 1–2 $\mathbf{m^{-1}}$, 2–3 $\mathbf{m^{-1}}$, 3–4 $\mathbf{m^{-1}}$, and 4–5 $\mathbf{m^{-1}}$ (Fig. 3.8 - e). The plan curvature values represented the steep degrees of slopes that influenced the characteristics of surface runoff contributing to terrain instability (Chen et al. 2019a). The plan curvature values were derived from the DEM and classified according to the natural break method into five groups: (-17.246)–(-3.024), (-3.024)–(-0.806), (-0.806)–(0.368), 0.368–1.803, and 1.803–16.025 (Fig. 3.8 - f). Profile curvature is the curvature in the vertical plane parallel to the slope direction (Yilmaz et al. 2012). The profile curvature values acquired through DEM were divided into five classes using the natural break

method: (-19.381)–(-2.218), (-2.218)–(-0.618), (-0.618)–(0.690), 0.690–2.726, and 2.726–17.708 (Fig. 3.8 - g). The geological map of the study area was obtained from the Geological Survey of Japan, AIST, and the lithology map was categorized as follows (Fig. 3.8 - h): (1) higher terrace; (2) lower terrace; (3) mafic plutonic rocks; (4) marine and non-marine sediments; (5) marine sedimentary rocks; (6) non-alkaline pyroclastic flow volcanic rocks; (7) swamp deposits; (8) ultramafic rocks; (9) water. The geological age map was divided into 12 classes as follows (Fig. 3.8 - i): (1) Early Miocene to Middle Miocene; (2) Early to Middle Miocene; (3) Late Cretaceous; (4) Late Eocene to Early Oligocene; (5) Late Miocene to Pliocene; (6) Late Pleistocene; (7) Late Pleistocene to Holocene; (8) Middle Eocene; (9) Middle Pleistocene; (10) Middle to Late Miocene; (11) Present; (12) Unknown age

The distance to fault was computed by a buffer operation. The distance to fault was classified by the geometrical interval function: 1-2.947 km, 2.947-5.545 km, 5.545-9.008 km, 9.008-13.627 km, 13.627-19.786 km, and more than 19.786 km (Fig. 3.8 - j). The distance to epicenter was divided according to natural breaks: 1-6 km, 6-11 km, 11-15 km, 15-19 km, 19-23 km, 23-27 km, 27-31 km, and 31-38 km (Fig. 3.8 - k). The values of PGA were divided into 10 categories using the geometrical interval function: 184–466 gal, 466–604 gal, 604-671 gal, 671-703 gal, 703-719 gal, 719-752 gal, 752-819 gal, 819-956 gal, 956-1,238 gal, and 1,238-1,817 gal (Fig. 3.8 - l). The values of PGA were acquired from K-NET station, Japan (http://www.kyoshin.bosai.go.jp/).
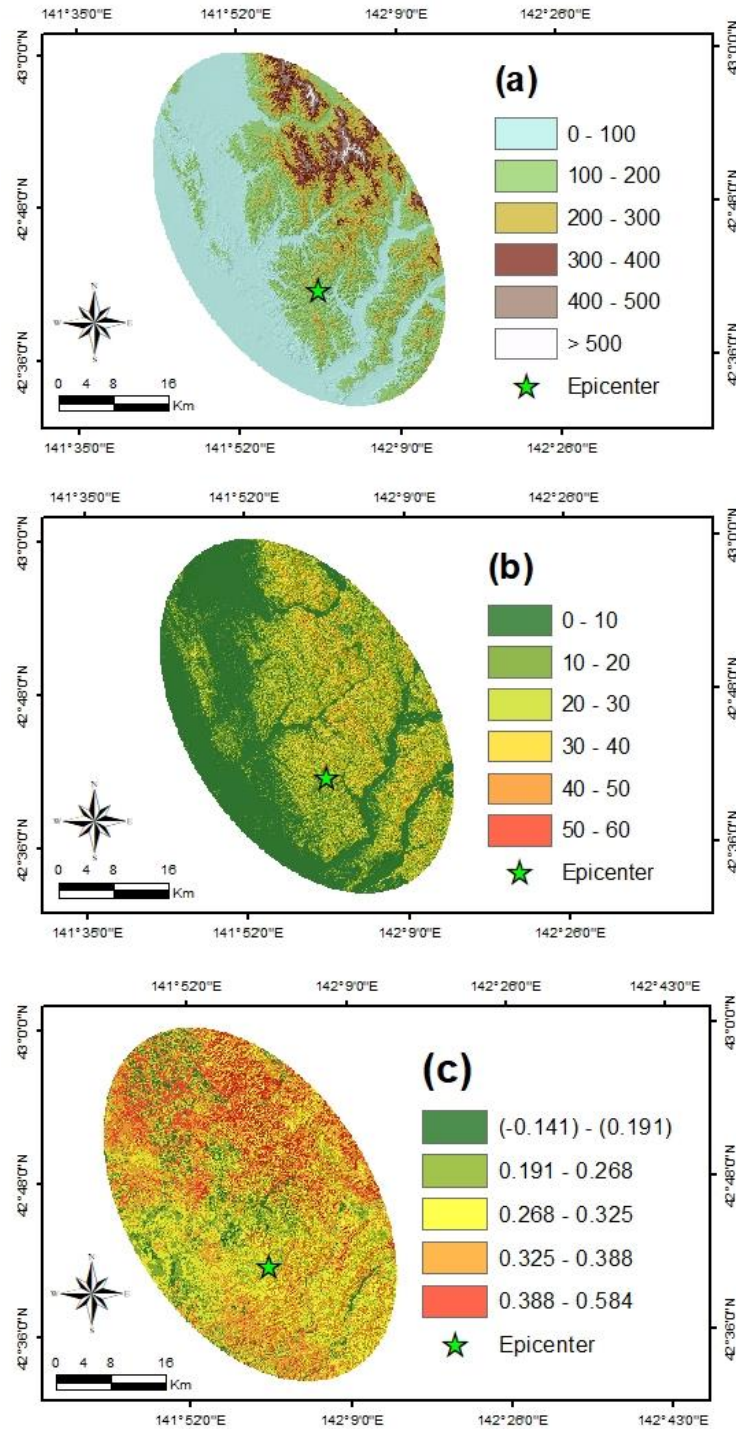
Fig. 3.8 Thematic maps of landslide-influencing factors in Iburi region of Hokkaido, Northern Japan: (a) elevation [m], (b) slope angle [degree], (c) NDVI, (d) distance to stream [m], (e) stream density [m^{-1}], (f) plan curvature, (g) profile curvature, (h) lithology, (i) geological age, (j) distance to fault [km], (k) distance to epicenter [km], (l) PGA [gal]

Fig. 3.8 continued

34
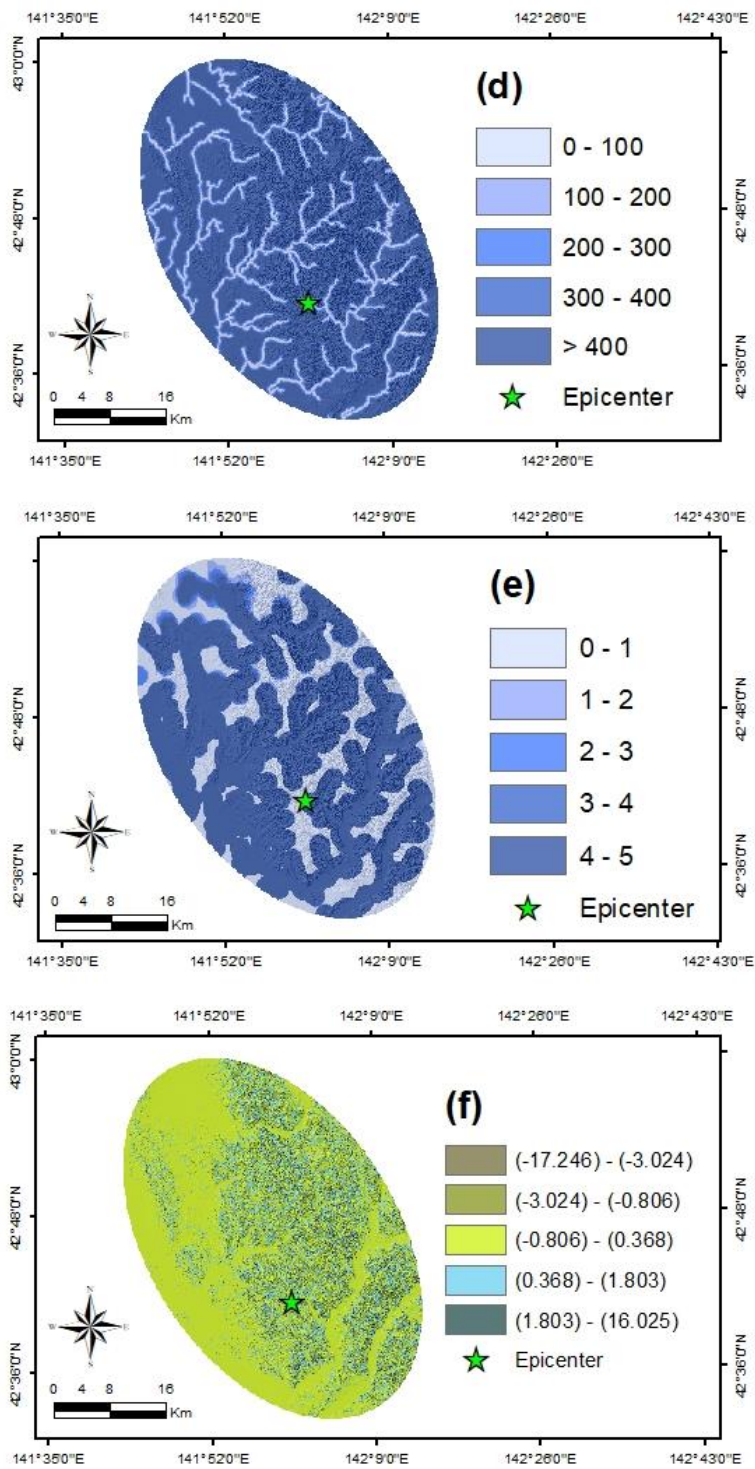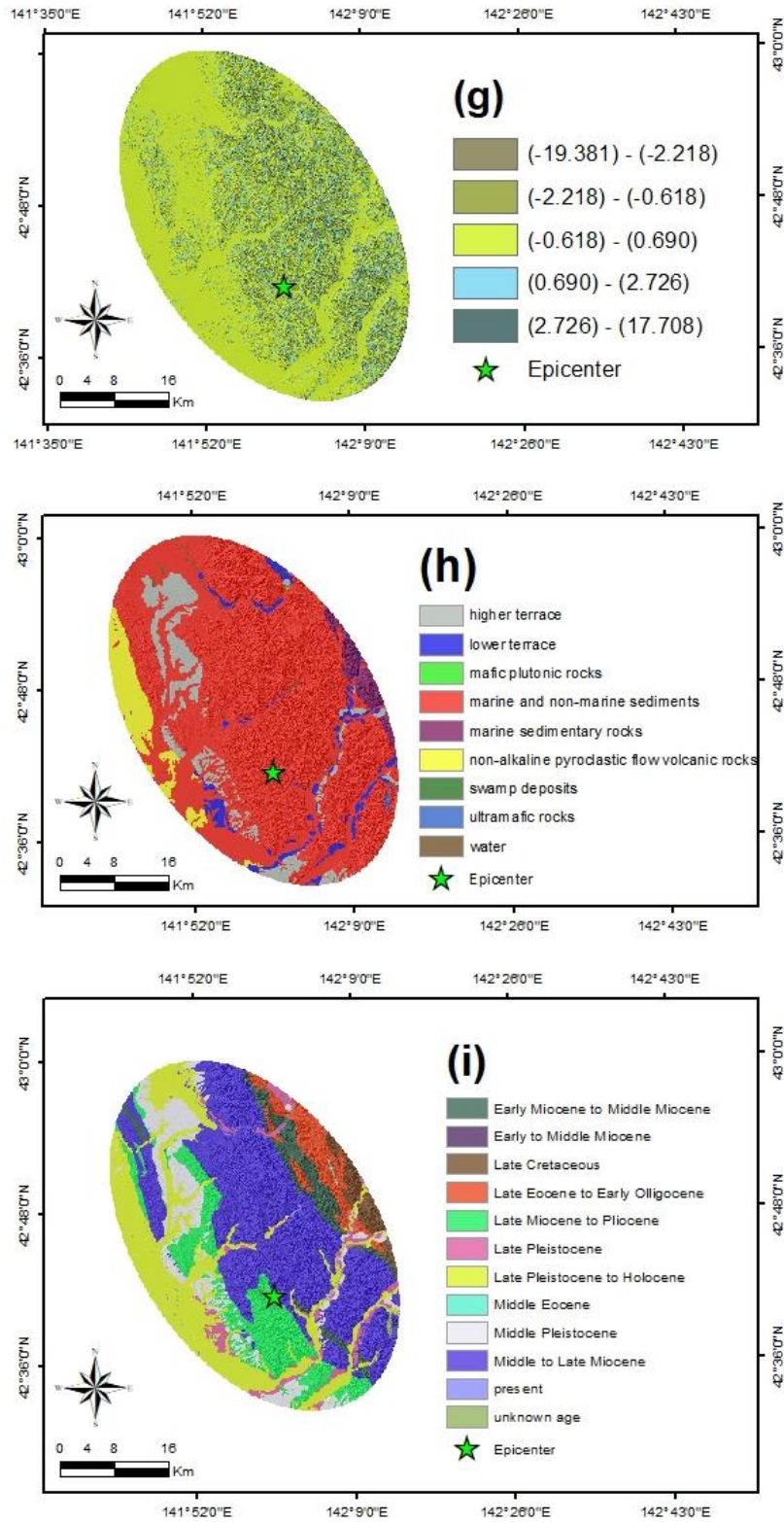
Fig. 3.8 continued
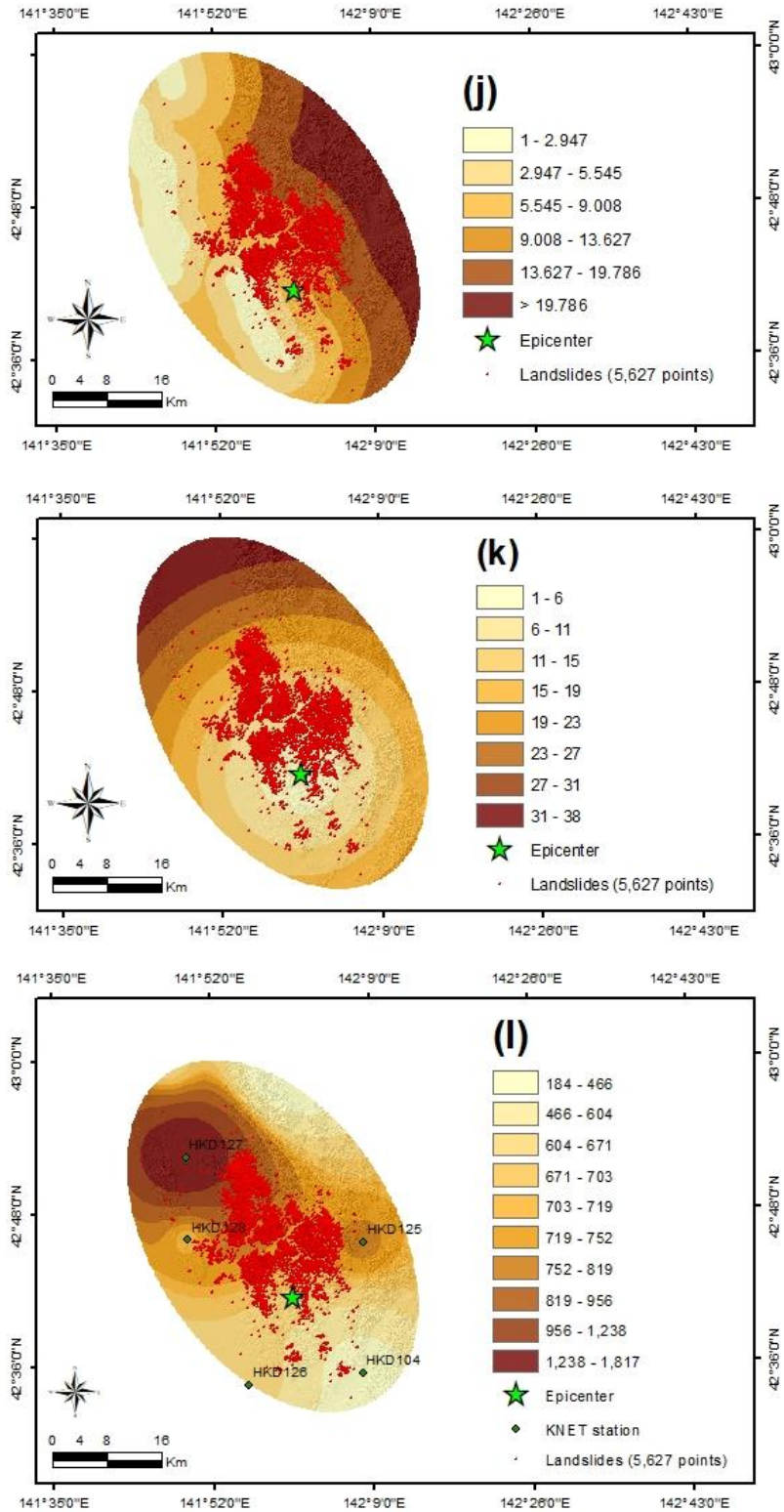
Fig. 3.8 continued

3.2 Results and discussion

3.2.1 Landslide susceptibility maps produced by stacked autoencoder

The final prediction results obtained from the autoencoder modeling were evaluated using the testing data set based on qualitative and quantitative analyses to validate the performance of the models. A flowchart of the proposed autoencoder framework is illustrated in Fig. 3.9. The autoencoder models based on the deep neural network were coded in R language on RStudio using H2O packages. These algorithms were performed using hyperbolic tangent function (i.e., the tanh function) in every hidden layer which was used to encode and decode the input to the output in the undercomplete autoencoder. In the H2O library, five hidden layers with encoders and decoders were designed by using the tanh activation function in each layer, which was composed of 10-5-2-5-10 (Fig. 3.10). The 12 landslide susceptibility maps derived from the autoencoder framework are shown in Fig. 3.11 and Fig. 3.12. It was observed that the accuracy increased with an increase in the sampling ratio, but the precision and recall curve decreased (Table 3.1). The 12 susceptibility maps showed different spatial distributions in landslide susceptibility. Both the PM 1 (Fig. 3.11 - a) model and the M 1 (Fig. 3.12 - a) model were predicted to be prone to landslides in most of the study area, indicating the over-estimation of landslide susceptibility and low capacity in distinguishing landslide-prone areas from stable areas. The PM 1 and M 1 models had the same accuracy of 89.2% by means of confusion matrix, while the precision and recall curve showed that the M 1 model had a performance of 94.1%, which was higher than the 93.7% of the PM 1 model. Regarding the PM 2 (Fig. 3.11 - b) and M 2 (Fig. 3.12 - b) models, the PM 2 model had an accuracy of 91.1% and a precision and recall curve of 93.8%, which was better than the M 2 model, indicating an accuracy of 89.4% and a precision and recall curve of 89.7%. In the PM 2 model and the M 1 model, the area under the curve of TPR and TNR, and TPR and FPR showed good performance. The PM 2 model with a sampling ratio of 1:2 had the best performance in both distinguishing landslide-prone areas and producing sound information on landslide susceptibility values. The M 1 model sampled on the mountainous zone showed lower accuracy performance compared with the PM 2 model sampled on the combination including plain and mountainous zone. However, the precision and recall curve had the best performance with high accuracy. Regarding the area under the curve on TPR and TNR, and TPR and FPR, the PM 3 model (Figs Fig. 3.11 - c), the PM 4 model (Fig. 3.11 - d), the PM 5 model (Fig. 3.11 - e), and the PM 6 model (Fig. 3.11

- f) distinguished the potential landslide areas from the stable areas without expanding the spatial extent of the potential landslide areas. The M 3 model (Fig. 3.12 - c), the M 4 model (Fig. 3.12 - d), the M 5 model (Fig. 3.12 - e), and the M 6 model (Fig. 3.12 - f) generated in the mountainous zone tended to detect stable areas as landslide susceptibility areas even though there were no source areas that caused landslides to be triggered by earthquakes. As shown in Fig. 3.13, the final landslide susceptibility index mapped five categories for the PM 2 model (Fig. 3.13 - a) and the M 1 model (Fig. 3.13 - b), which were the best models selected regarding accuracy and the area under the curve in precision and recall, TPR and TNR, and TPR and FPR. The predictive capability of all factors that influenced the landslides was evaluated using the test dataset based on H2O's deep learning algorithm (Gedeon 1997), which is a methodology for computing variable importance. Table 3.2 and Table 3.3 lists the results of the analysis of the variable importance of the factors that influenced the landslides in H2O's deep neural network. In general, the results showed that the earthquake dataset, such as distance to fault, distance to epicenter, and PGA was of high importance to the models, whereas the geomorphology, including slope, plan curvature, profile curvature, stream density, and distance to stream, had lower predictive capability in both areas. Furthermore, in the PM 1 model, the lithology of the geology dataset as categorical variables indicated the highest importance in the models.
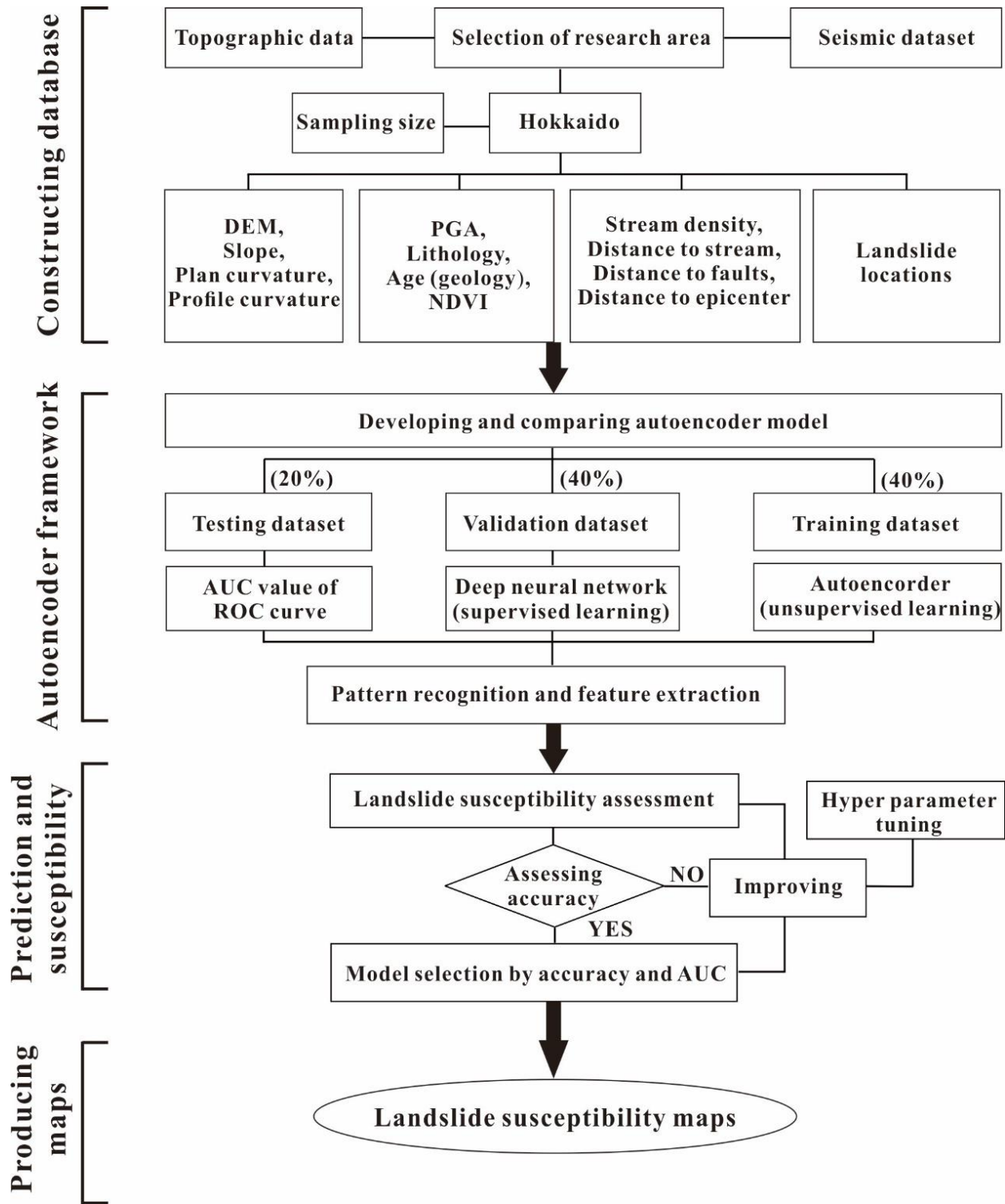
Fig. 3.9 Flow chart of the research process
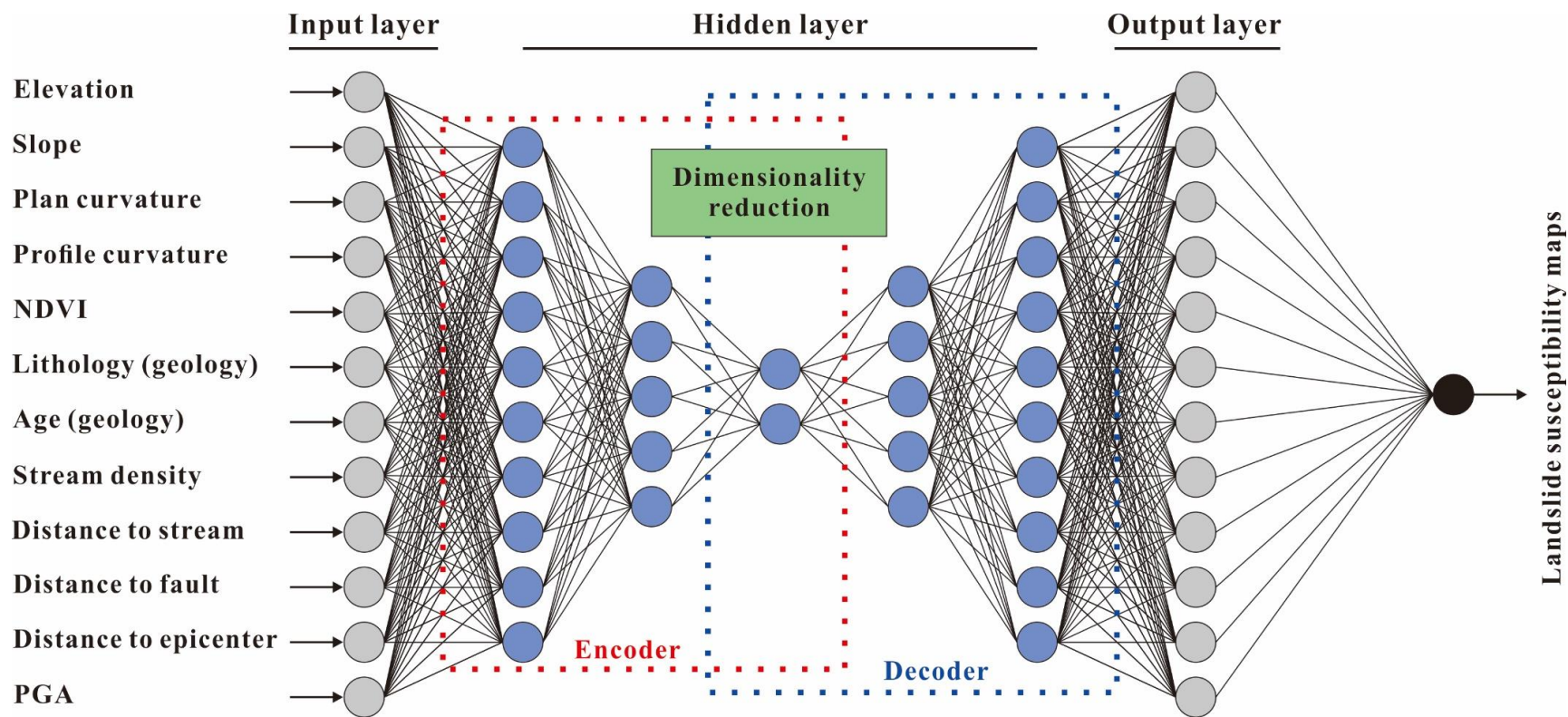
Fig. 3.10 Diagram of autoencoder based on deep neural network with five hidden layers used in this study

Table 3.1 The area under the curve and accuracy of models' responses in sampling ratios for the combination zone including plain and mountain (PM) and for the mountainous only zone (M)

Zone	Model	Sampling ratio (Sampling numbers)	Area under the curve on test data set			Accuracy
			Precision & Recall	TPR & TNR	TPR & FPR	
Combination zone including plain and mountain (PM)	**PM 1**	1:1 (5627:5627)	0.937	0.948	0.891	0.892
	PM 2	**1:2 (5627:11254)**	**0.938**	**0.968**	**0.907**	**0.911**
	PM 3	1:3 (5627:16881)	0.903	0.967	0.915	0.920
	PM 4	1:4 (5627:22508)	0.833	0.957	0.905	0.916
	PM 5	1:5 (5627:28135)	0.854	0.967	0.911	0.932
	PM 6	1:10 (5627:56270)	0.754	0.964	0.910	0.943
Mountainous zone (M)	**M 1**	**1:1 (5627:5627)**	**0.941**	**0.951**	**0.891**	**0.892**
	M 2	1:2 (5627:11254)	0.897	0.952	0.886	0.894
	M 3	1:3 (5627:16881)	0.872	0.952	0.887	0.894
	M 4	1:4 (5627:22508)	0.845	0.949	0.881	0.910
	M 5	1:5 (5627:28135)	0.800	0.949	0.883	0.918
	M 6	1:10 (5627:56270)	0.710	0.956	0.893	0.940
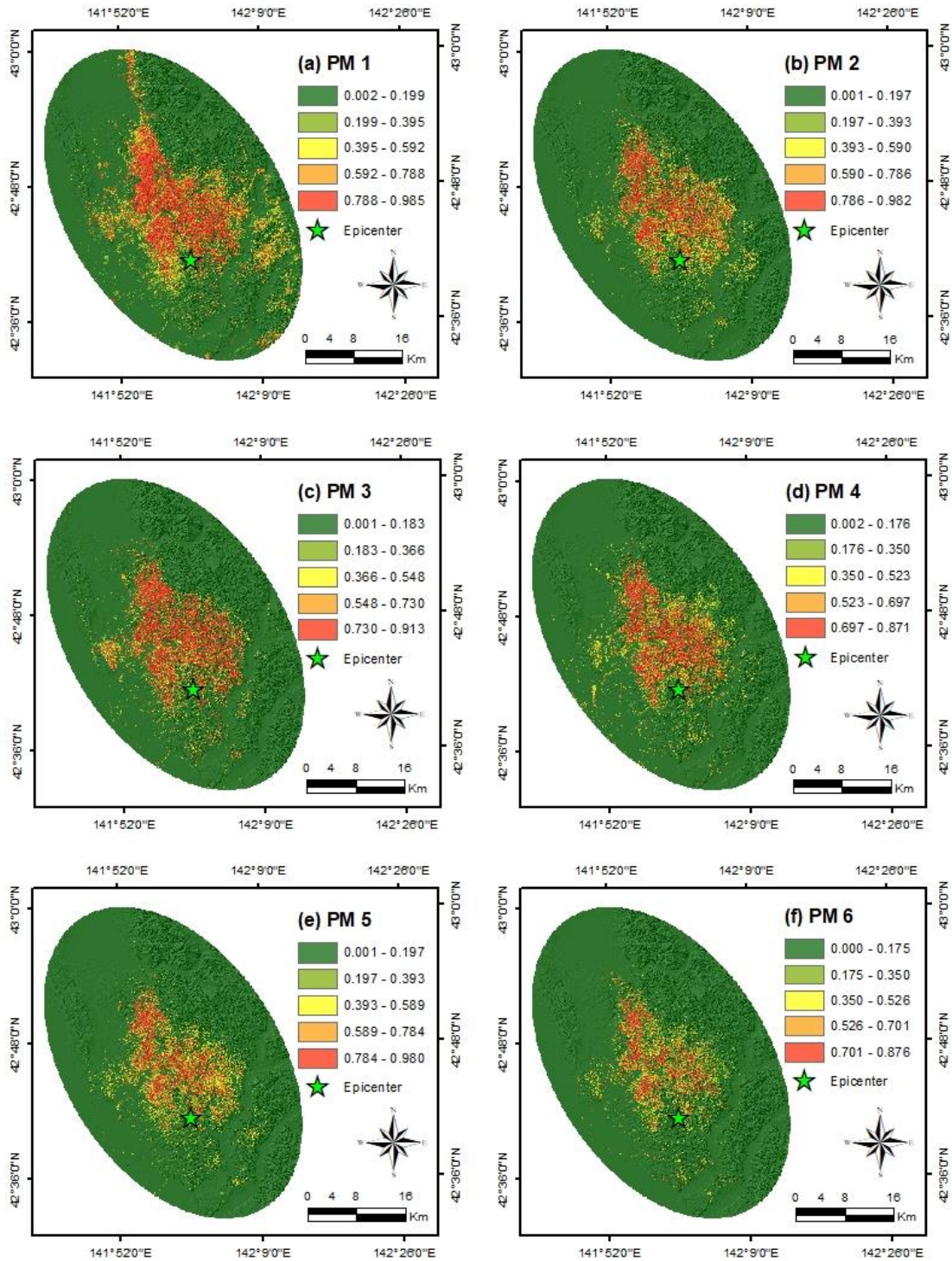
Fig. 3.11 Landslide susceptibility assessment on sampling strategies of non-landslide points randomly generated in the combination zone including plain and mountain (PM): (a) PM 1, (b) PM 2, (c) PM 3, (d) PM 4, (e) PM 5, and (f) PM 6
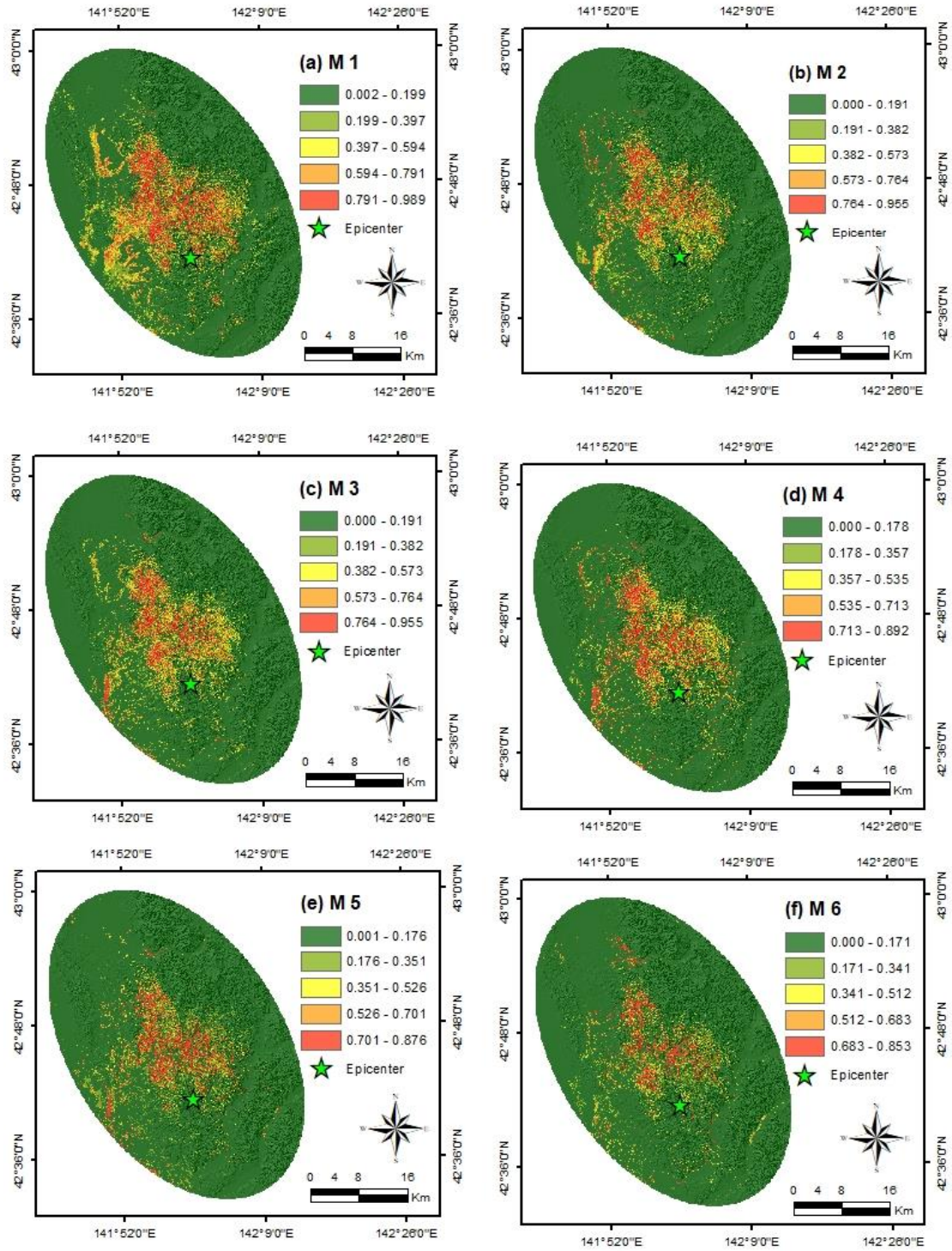
Fig. 3.12 Landslide susceptibility assessment on sampling strategies of non-landslide points randomly generated in the mountainous only zone (M): (a) M 1, (b) M 2, (c) M 3, (d) M 4, (e) M 5, and (f) M 6
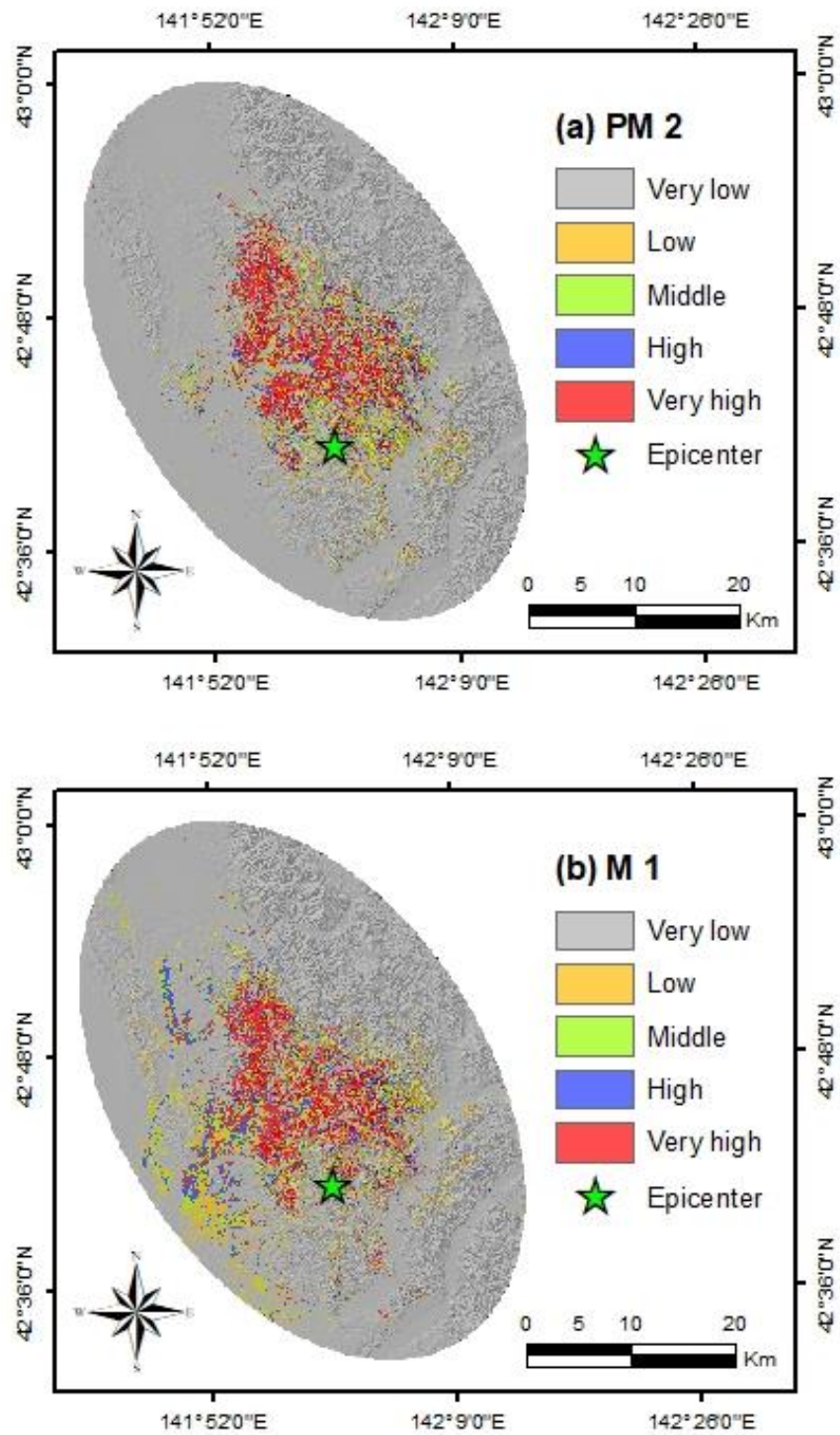
Fig. 3.13 Landslide susceptibility maps of best performance selected from both PM and M models considering the accuracy and the area under the curve on Precision & Recall, TPR & TNR, and TPR & FPR: (a) PM 2, (b) M 1

Table 3.2 Variable importance and ranking for the combination zone including plain and mountain (PM)

Variable factors	Variable importance of the combination zone including plain and mountain (PM)											
	PM 1	Ranking	PM 2	Ranking	PM 3	Ranking	PM 4	Ranking	PM 5	Ranking	PM 6	Ranking
Elevation	0.065	9	0.104	4	0.098	5	0.058	9	0.073	7	0.057	9
Slope	0.076	7	0.088	5	0.068	8	0.072	8	0.071	8	0.089	5
Plan curvature	0.028	12	0.027	12	0.016	12	0.022	11	0.023	12	0.024	12
Profile curvature	0.041	11	0.040	11	0.031	11	0.020	12	0.034	11	0.024	11
NDVI	0.067	8	0.074	9	0.081	7	0.053	10	0.100	4	0.077	7
Lithology (geology)	0.263	1	0.080	6	0.121	3	0.113	4	0.082	5	0.108	4
Age (geology)	0.096	3	0.077	7	0.084	6	0.118	3	0.041	10	0.087	6
Stream density	0.058	10	0.075	8	0.066	9	0.103	5	0.082	6	0.072	8
Distance to stream	0.085	5	0.045	10	0.042	10	0.085	6	0.056	9	0.049	10
Distance to fault	0.138	2	0.117	3	0.108	4	0.138	2	0.157	1	0.132	2
Distance to epicenter	0.082	6	0.135	2	0.144	1	0.141	1	0.140	2	0.171	1
PGA	0.096	4	0.139	1	0.140	2	0.077	7	0.140	3	0.108	3

Table 3.3 Variable importance and ranking for the mountainous only zone (M)

Variable factors	Variable importance of the mountainous zone (M)											
	M 1	Ranking	M 2	Ranking	M 3	Ranking	M 4	Ranking	M 5	Ranking	M 6	Ranking
Elevation	0.080	7	0.075	6	0.067	7	0.090	5	0.065	9	0.071	7
Slope	0.068	9	0.070	7	0.039	10	0.049	8	0.037	10	0.034	10
Plan curvature	0.021	12	0.032	12	0.025	11	0.034	11	0.027	11	0.031	11
Profile curvature	0.044	11	0.033	11	0.021	12	0.033	12	0.021	12	0.024	12
NDVI	0.099	5	0.113	4	0.074	6	0.111	4	0.129	2	0.095	4
Lithology (geology)	0.085	6	0.104	5	0.105	4	0.082	6	0.091	7	0.095	5
Age (geology)	0.114	2	0.069	8	0.091	5	0.072	7	0.095	5	0.093	6
Stream density	0.072	8	0.058	9	0.058	8	0.045	10	0.089	8	0.067	8
Distance to stream	0.063	10	0.057	10	0.057	9	0.047	9	0.095	5	0.044	9
Distance to fault	0.109	4	0.124	2	0.170	1	0.166	1	0.107	4	0.162	2
Distance to epicenter	0.134	1	0.144	1	0.167	2	0.150	2	0.127	3	0.103	3
PGA	0.110	3	0.120	3	0.126	3	0.121	3	0.149	1	0.181	1

3.2.2 Validation on landslide susceptibility prediction in Hokkaido

The 12 landslide susceptibility maps produced by the autoencoder framework were evaluated by the area under the curve in precision and recall, TPR and TNR, and TPR and FPR. In the PM 1 and M 1 models, the spatial distributions of landslide susceptibility were much higher than in the other models. The susceptibility values were mainly distributed around the two opposite extremes between 0 and 1. The PM 2 model had better precision, recall, sensitivity, specificity, and overall accuracy than other models did. In both regions, the models with sampling sizes greater than 1:3 showed poor classification performance (Table 3.1). The landslide susceptibility maps were produced differently depending on the sampling size used and the area selected. The sampling size and the area selected in PM and M may have affected various prediction abilities. In this study, the sampling size and the area resulted in different contributions to the models. In the autoencoder method, the sampling ratio of 1:2 in the non-landslide points generated in the PM and M improved the prediction accuracy of landslide susceptibility mapping. The autoencoder effectively extracted a feature selection of spatial patterns using dimensionality reduction, and it significantly reduced the number of network parameters. Deep learning techniques could be used to explore the representation needed for making predictions based on raw data. Therefore, a promising avenue of research is to explore the probability of applying powerful deep learning methods to landslide susceptibility mapping (Wang et al. 2019). Moreover, various sampling strategies present varying accuracy in landslide susceptibility mapping, and it is recommended that sampling strategies be considered in applying new statistical techniques.

Landslides triggered by 2013 extreme rainfall

in Shimane Prefecture

In this chapter, autoencoder models are compared with conventional machine learning both support vector machine and random forest models which is well known as good performance for landslide susceptibility prediction. As a case study for landslides triggered by extreme rainfall, the landslide dataset in Oda City and Gotsu City in Shimane Prefecture, southwestern Japan is used. The results show that classifiers that combine both autoencoder and random forest are better predictive performance than single classifiers.

4.1 Study area

The study area is located in Oda City and Gotsu City, Shimane Prefecture, southwestern Japan (Fig. 4.1). The elevation varies from sea level to 1,123 m (Table 4.1). The average annual precipitation recorded from the rainfall station of Fukumitsu, Oda, and Sakurae are 1657, 1786, and 2011 mm from 2008 to 2018 (Fig. 4.2). The cumulative rainfall of 2013 recorded from the rainfall station of Fukumitsu, Oda, and Sakurae are 2270, 2102, and 2656 mm, respectively (http://www.jma.go.jp/). In this study, a total of 90 landslides were caused by extreme rainfall from May to October 2013 (Table 4.2), especially 69 of landslides triggered by extreme rainfall in August 2013. These landslides can be mainly described as shallow landslides that were determined based on field investigation.

4.1.1 Landslide inventory and spatial database

Landslide susceptibility prediction can be evaluated as a binary classification problem between landslides and non-landslides. A spatial database setting including landslide pixel grid, non-landslide pixel grid, and related landslide affecting factors is needed for statistical analysis (Huang

et al. 2019). This spatial database was divided into a training dataset and a validation dataset. These real 90 of landslides and 90 of non-landslides artificially generated from ArcGIS software were randomly split into two parts with a ratio of 70 % and 30 %. The 70 % of landslide and non-landslide grid cells were selected for training model, and the remainder 30% was used for validation model. Furthermore, the landslide (event) and non-landslide (non - events) grid cells were set to 1 and 0 respectively, and the values of 1 and 0 were used for classification and prediction as the output variables of landslide susceptibility prediction models.
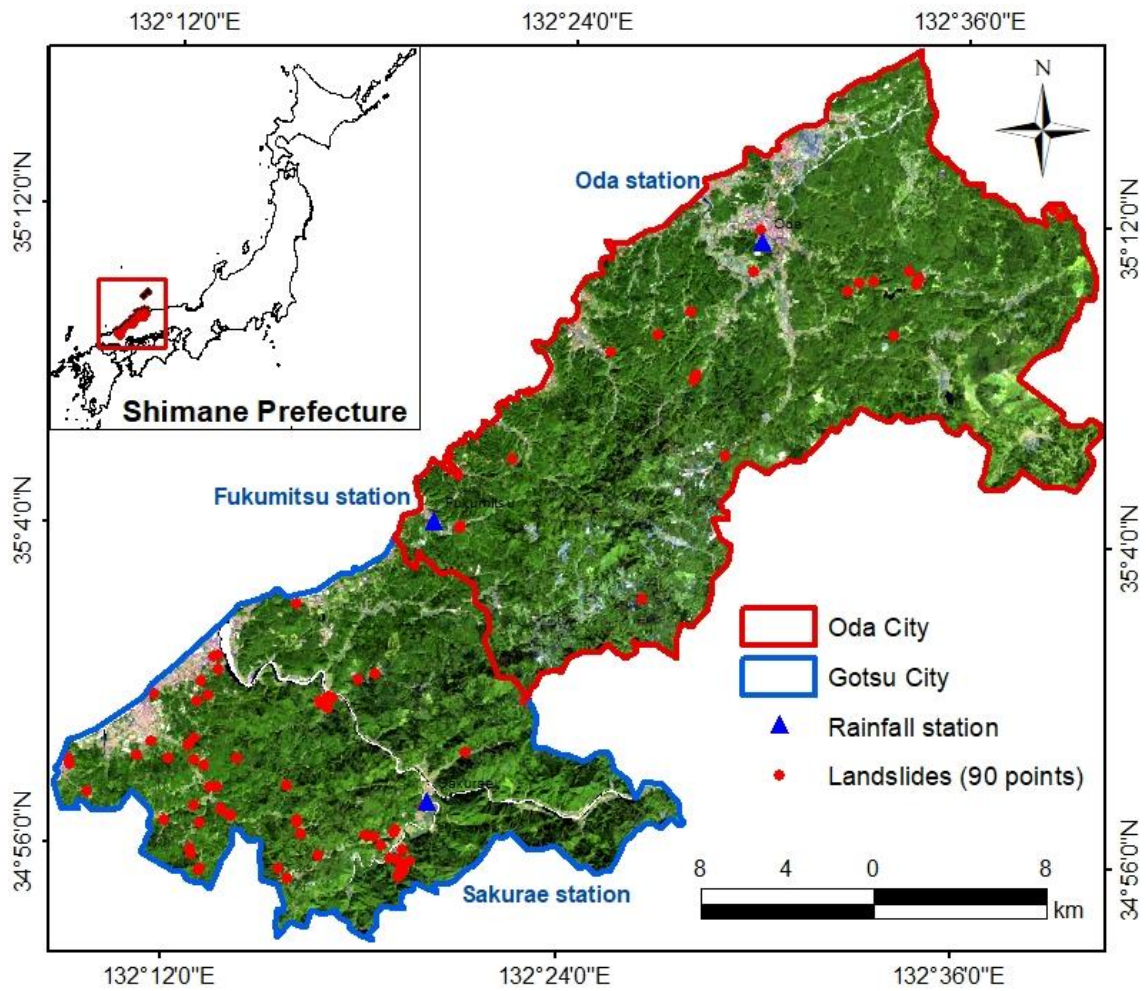
Fig. 4.1 Study area and landslide inventory of Oda City and Gotsu City in Shimane Prefecture, southwestern Japan

Annual rainfall chart (2008–2018):

	2008	2009	2010	2011	2012	2013	2014	2015	2016	2017	2018
Fukumitsu	1419	1843	1618	1733.5	1365.5	2270.5	1446.5	1444	1780.5	1560	1747
Oda	1563	1905.5	1671	1858	1434	2102	1706	1860	1969	1678	1899.5
Sakurae	1855.5	2023	1882.5	2167.5	1677.5	2656.5	1841.5	1888.5	2107.5	1931	2100.5

Monthly rainfall chart (2013):

	Jan.	Feb.	Mar.	Apr.	May	June	July	Aug.	Sep.	Oct.	Nov.	Dec.
Fukumitsu	71	74	80.5	113.5	51.5	302.5	349	526	196.5	243.5	123	139.5
Oda	88.5	82	96.5	155	64.5	284	272	288.5	182.5	247	165.5	176
Sakurae	111	97	67.5	161.5	59.5	287	399.5	604.5	209.5	263	151	245.5

Fig. 4.2 Annual rainfall from 2008 to 2018, and monthly rainfall of 2013 in the study area

Table 4.1 Description and frequency ratio (FR) of topographical and distance to factors in the study area

Factors	Values	No. of Landslides	FR	Factors	Values	No. of Landslides	FR
Altitude (m)	0 - 105.77	59	2.15	**Profile curvature**	-37.55 - (-3.71)	3	0.84
	105.78 - 215.95	21	0.80		-3.72 - (-1.18)	6	0.43
	215.96 - 339.36	10	0.43		-1.19 - 1.03	39	0.90
	339.37 - 550.90	0	0		1.04 - 3.87	36	1.53
	550.91 - 1,123.84	0	0		3.88 - 43.08	6	1.06
Slope (degree)	0 - 9.50	2	0.78	**Dis. to stream**	< 101	58	1.64
	9.51 - 19.00	30	1.11		101 - 200	21	0.73
	19.01 - 28.21	29	1.08		201 - 300	8	0.44
	28.22 - 38.00	24	0.92		301 - 400	3	0.46
	38.01 - 73.40	5	0.71		> 401	0	0
Plan curvature	-49.05 - (-3.81)	2	0.78	**Dis. to road**	< 200	39	2.91
	-3.82 - (-1.11)	12	1.11		201 - 400	17	1.38
	-1.12 - 0.57	47	1.08		401 - 600	7	0.64
	0.58 - 2.60	24	0.92		601 - 800	5	0.52
	2.61 - 37.03	5	0.71		> 801	22	0.50

Table 4.2 Description and frequency ratio (FR) of remote sensing - derived index and hydrological factors in the study area

Factors	Values	No. of Landslides	FR	Factors	Values	No. of Landslides	FR
NDVI	-0.242 - 0.143	15	7.26	**SPI**	-13.816 - (-8.806)	3	0.65
	0.144 - 0.255	19	3.15		-8.805 - (-4.352)	14	0.83
	0.256 - 0.332	30	1.40		-4.351 - 0.101	20	0.76
	0.333 - 0.391	26	0.75		0.102 - 2.773	46	1.28
	0.392 - 0.650	0	0		2.774 - 14.574	7	1.04
NDWI	-0.324 - 0.046	1	0.22	**TWI**	-7.969 - (-2.240)	17	0.82
	0.047 - 0.125	22	2.19		-2.239 - 2.114	23	0.75
	0.126 - 0.179	36	1.75		2.115 - 4.520	38	1.43
	0.180 - 0.223	25	0.79		4.521 - 8.416	12	1.22
	0.224 - 0.483	6	0.26		8.417 - 21.250	0	0
BI	0.248 - 0.312	4	0.86	**Rainfall (mm)**	1,338.5 - 1,424	13	0.54
	0.313 - 0.322	10	0.45	**(from May to Oct. in 2013)**	1,424.1 - 1,528.5	5	0.36
	0.323 - 0.329	33	0.97		1,528.6 - 1,633	2	0.17
	0.330 - 0.339	34	1.50		1,633.1 - 1,718.5	47	1.69
	0.340 - 0.436	9	1.41		1,718.6 - 1,823	23	1.82

4.1.2 Landslide affecting factors in Shimane Prefecture

The landslide affecting factors in a certain study area are complex, and it is difficult to confirm which affecting factors are the most important and necessary among the topographic, geological, hydrological, and distance to factors (Huang et al. 2019). In landslide susceptibility modeling, landslides may reoccur under conditions similar to past landslides (Westen et al. 2003; Lee and Talib, 2005; Dagdelenler et al. 2016). A total of 14 affecting factors were acquired and chosen as input variables for landslide susceptibility models (Fig. 4.3, 4.4, and 4.5). The topographic factors were acquired (https://fgd.gsi.go.jp) and calculated based on the digital elevation model (DEM), with a spatial resolution of 10 m including altitude, slope angle, plan curvature, profile curvature (Yilmaz et al. 2012), distance to stream (Devkota et al. 2013; Guo et al. 2015), stream power index (SPI) (Park and Kim, 2019), and topographic wetness index (TWI) (Althuwaynee et al. 2016; Colkesen et al. 2016). The distance to road (Alexakis et al. 2014; Roy et al. 2019) was acquired from Geospatial Information Authority of Japan (www.gsi.go.jp). The remote sensing - derived indexes were extracted from the Landsat TM 8 (https://earthexplorer.usgs.gov/), resampled with a 10 m resolution (Zhu et al. 2018): normalized difference vegetation index (NDVI) (Chen et al. 2019a), normalized different water index (NDWI) (Luo et al. 2019), bare soil index (BI) (Huang et al. 2019). The geological factors derived from geological map with a scale of 1:200,000 were obtained from the Geological Survey of Japan, AIST (https://www.gsj.jp/en/). These landslide affecting factors were reflected using the raster format with a spatial resolution of 10×10 m, which results in raster format that has the advantages of regular shape, quick subdivision, and high modeling efficiency (Huang et al. 2019). For continuous affecting factors, the 'Jenks natural break' method was used to divide each continuous affecting factor into five classes. Then the frequency ratio of all subclasses of each landslide affecting factor was calculated as shown in (Table 4.1, 4.2 and 4.3). The frequency ratio allows that all 14 of landslide affecting factors have significant influences on landslide occurrence. Some studies have suggested that the correlations between affecting factors should be eliminated to reduce model noise for the landslide susceptibility assessment (Hong et al. 2017; Lin et al. 2017; Chen et al. 2018a). However, the number of input variables of the deep learning algorithm is generally hundreds or thousands due to their strong feature extraction ability, and 14 input variables will not result in information redundancy. On the other hand, some collinearity phenomena between landslide affecting factors can be tolerated by the fast-developed machine learning models (Huang et al. 2019). These 14 of landslide affecting

factors provide valuable information to produce landslide susceptibility maps, as quantitative measurement determined by frequency ratio. Therefore, all 14 environmental factors are utilized as input variables in the model to evaluate the capabilities of performance and feature extraction for the landslide susceptibility assessment.
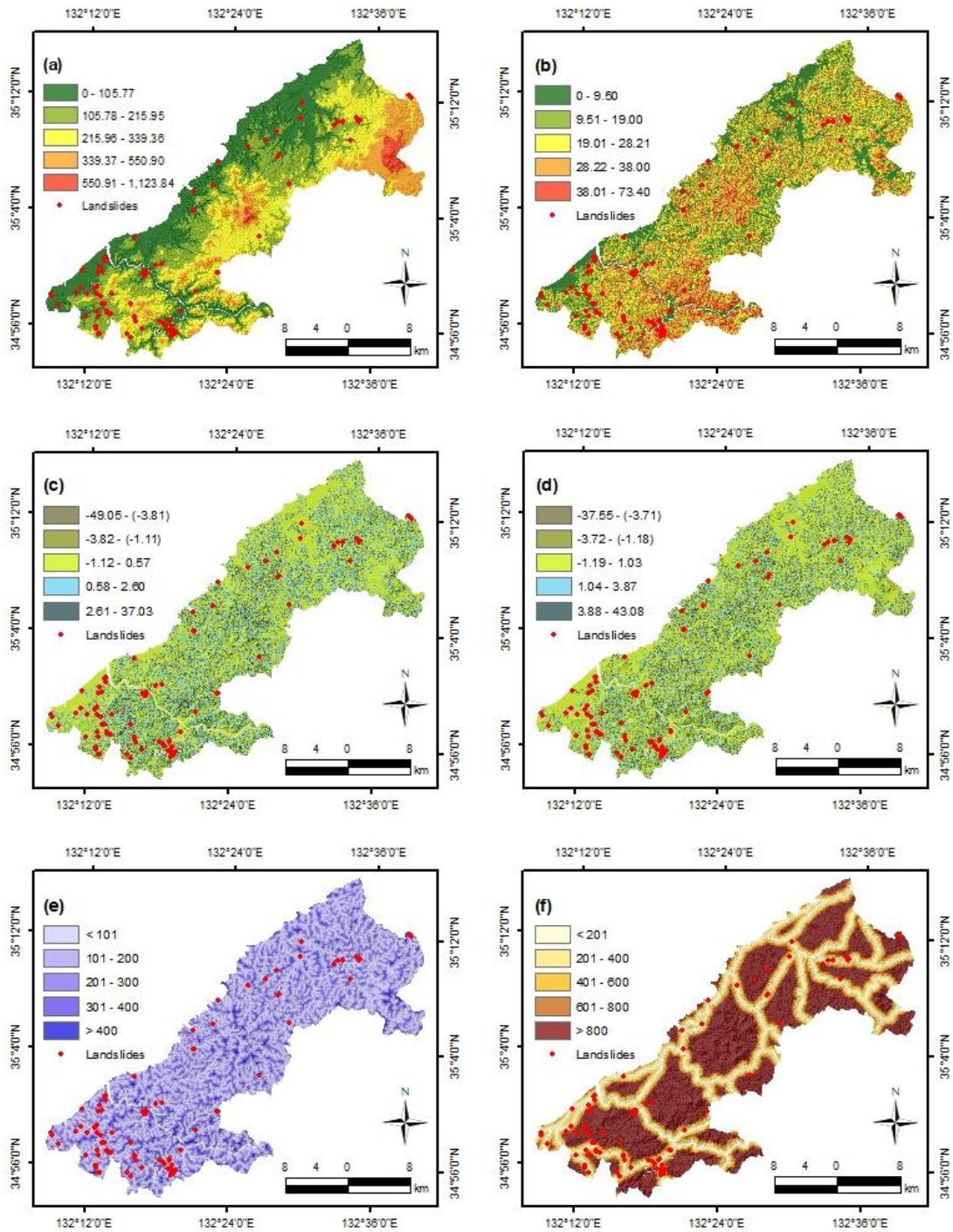
Fig. 4.3 Thematic maps of topographic factors (a - d) and distance to factors (e and f) considered in this study: (a) elevation [m], (b) slope angle [degree], (c) plan curvature, (d) profile curvature, (e) distance to stream [m], and (f) distance to road [m]
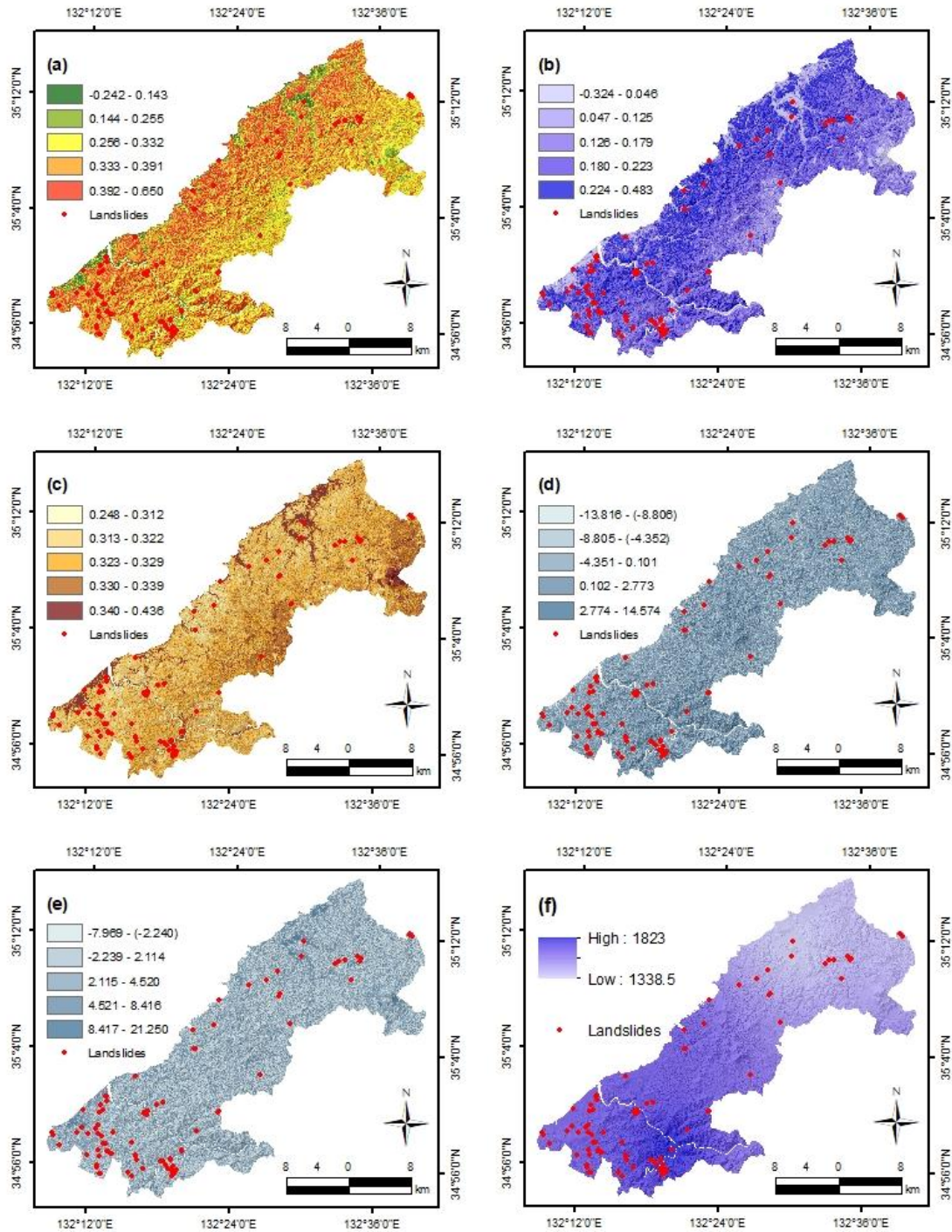
Fig. 4.4 Thematic maps of remote sensing – derived index (a - c) and hydrological factors (d - f) considered in this study: (a) NDVI, (b) NDWI, (c) BI, (d) SPI, (e) TWI, and (f) cumulative rainfall from March to October [mm]
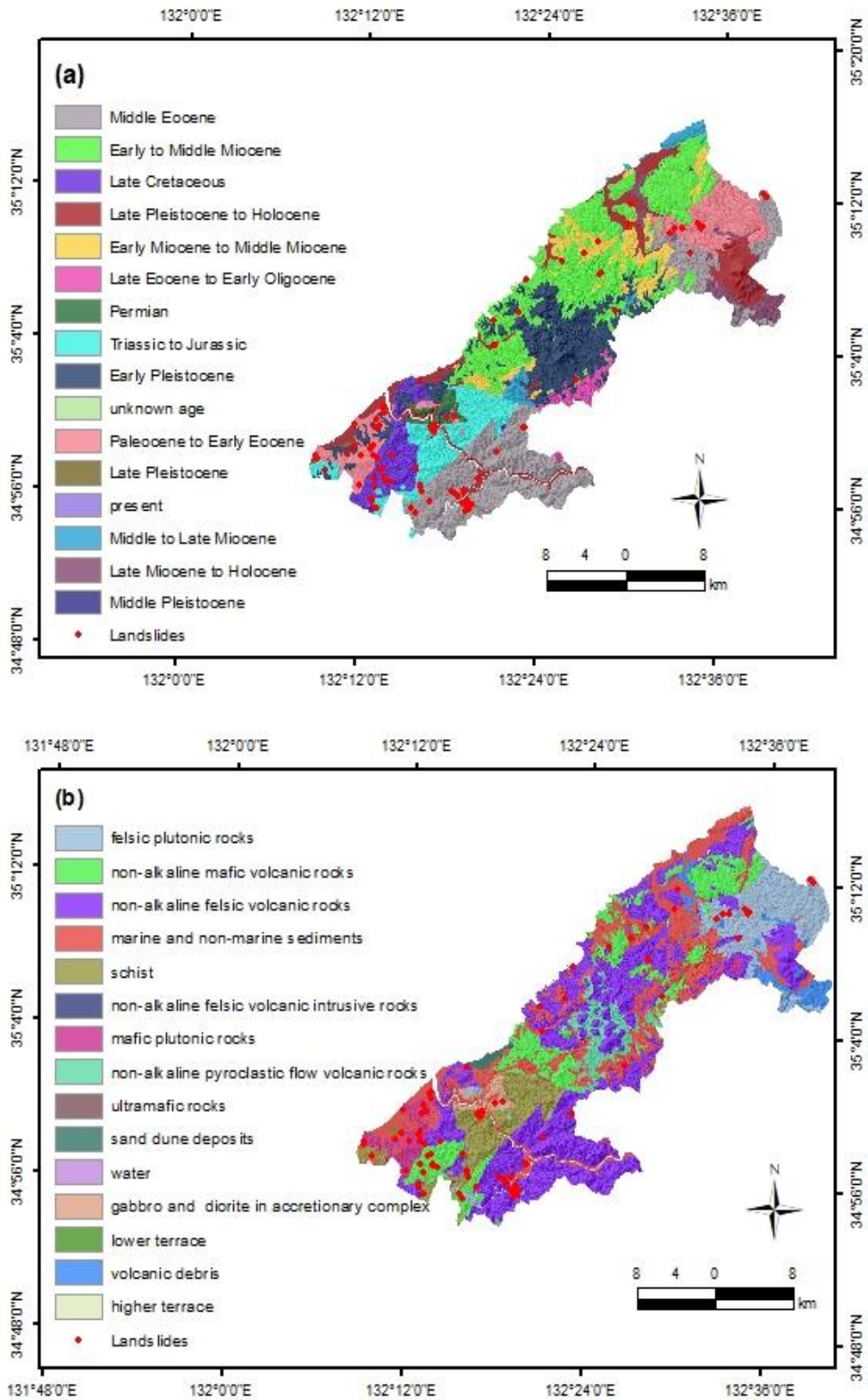
Fig. 4.5 Thematic maps of geological factors considered in this study: (a) geological age and (b) lithology

Table 4.3 Description and frequency ratio (FR) of geological factors in the study area

Factors	Values	No. of Ls	FR	Factors	Values	No. of Ls	FR
Geological age	Unknown age	22	**1.31**	**Lithology**	Felsic plutonic rocks	9	0.93
	Triassic to Jurassic	8	0.41		Gabbro and diorite in accretionary complex	13	**1.12**
	Present	14	**3.09**		Higher terrace	27	0.85
	Permian	13	**1.53**		Lower terrace	16	0.82
	Paleocene to Early Eocene	2	0.36		Mafic plutonic rocks	10	**1.50**
	Middle to Late Miocene	2	**1.37**		Marine and non-marine sediments	13	**3.94**
	Middle to Late Miocene	10	**9.15**		Non-alkaline felsic volcanic intrusive rocks	2	0.64
	Middle Eocene	1	0.15		Non-alkaline felsic volcanic rocks	0	0
	Late Pleistocene to Holocene	18	**1.41**		Non-alkaline mafic volcanic rocks	0	0
	Late Pleistocene	0	0		Non-alkaline pyroclastic flow volcanic rocks	0	0
	Late Miocene to Holocene	0	0		Sand dune deposits	0	0
	Late Eocene to Early Oligocene	0	0		Schist	0	0
	Late Cretaceous	0	0		Ultramafic rocks	0	0
	Early to Middle Miocene	0	0		Volcanic debris	0	0
	Early Pleistocene	0	0		Water	0	0
	Early Miocene to Middle Miocene	0	0			0	0

4.2 Results and discussion

4.2.1 Landslide susceptibility maps produced by six models

This study was performed using the following main steps (Fig. 4.6): (1) correlation analysis between landslide inventory and landslide affecting factors using frequency ratio, (2) landslide susceptibility prediction using SVM and RF models in machine learning, (3) landslide susceptibility prediction using StAE and SpAE employing back propagation neural network in deep learning, (4) evaluation of StAE and SpAE combined with machine learning acquired from a better prediction ratio between SVM and RF, and (5) validation and comparison. All models based on the deep learning and machine learning were coded in R language on RStudio. For the SVM model and RF model, its parameters are determined using a 10-fold cross-validation approach. The results show SVM model with radial basis function are acquired from grid search for SVM parameter tuning. For RF model, it is composed of 'mtry' and 'tree', which are 3 and 300, respectively. In the H2O library, both StAE and SpAE algorithms were performed using hyperbolic tangent function (i.e., the tanh function) in every hidden layer which was used to encode and decode the input to the output in the autoencoder framework. Both encoders and decoders were designed by using the tanh activation function in each hidden layer, which was composed of 80 - 50 - 2 - 50 - 80 for StAE (Fig. 4.7) and 200 - 200 - 200 for SpAE (Fig. 4.8) with parameter tuning. For combining models, reconstruction error value employing mean square error was used in both StAE and SpAE, which are 0.068 and 0.088, respectively. The landslide susceptibility maps derived from SVM, RF, StAE, SpAE, StAE with RF, and SpAE with RF model in the ArcGIS 10.6 software (Fig. 4.9). For better visualization and comparison, the indices were reclassified into five classes using the equal interval function: very low (0 - 0.2), low (0.2 - 0.4), moderate (0.4 - 0.6), high (0.6 - 0.8), and very high (0.8 - 1). The susceptibility class area of StAE model as the best performance (Table 4.4) were 6.31 %, 13.58 %, 33.04 %, 36.81 %, and 10.26 %, respectively. The susceptibility class area of RF model (Fig. 4.9 - b) and StAE model (Fig. 4.9 - c) has very high value. The susceptibility index value of SVM model (Fig. 4.9 - a) and StAE models (Fig. 4.9 - c) were prominent near the road (Fig. 4.3 - f). The SpAE model has lowest value in susceptibility class area (Fig. 4.9 - d). The StAE with RF model and SpAE with RF model by combined classifier were similar and has the lowest value in susceptibility class area (Fig. 4.9 - e and Fig. 4.9 - f).
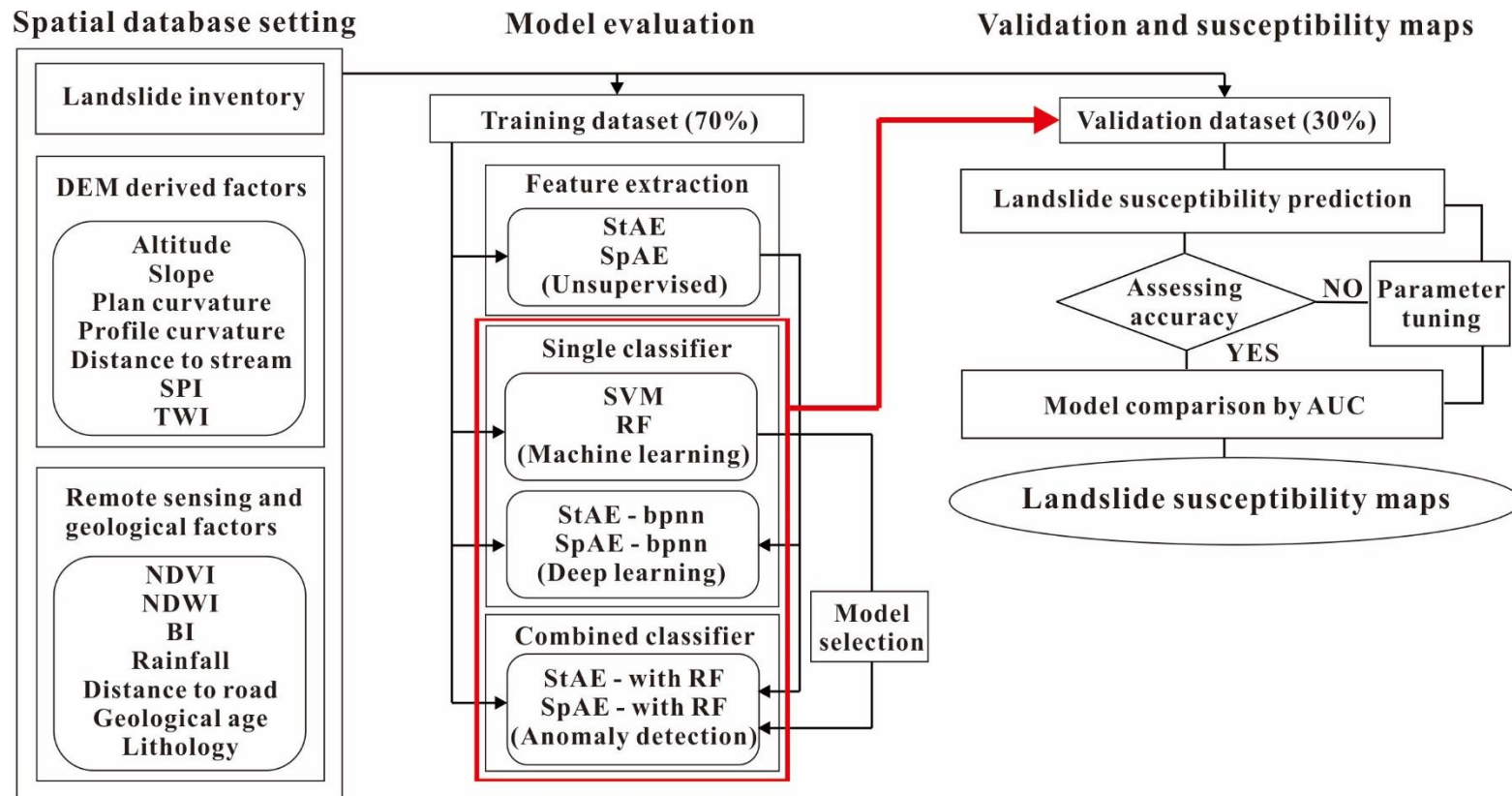
Fig. 4.6 Flow chart of the research process
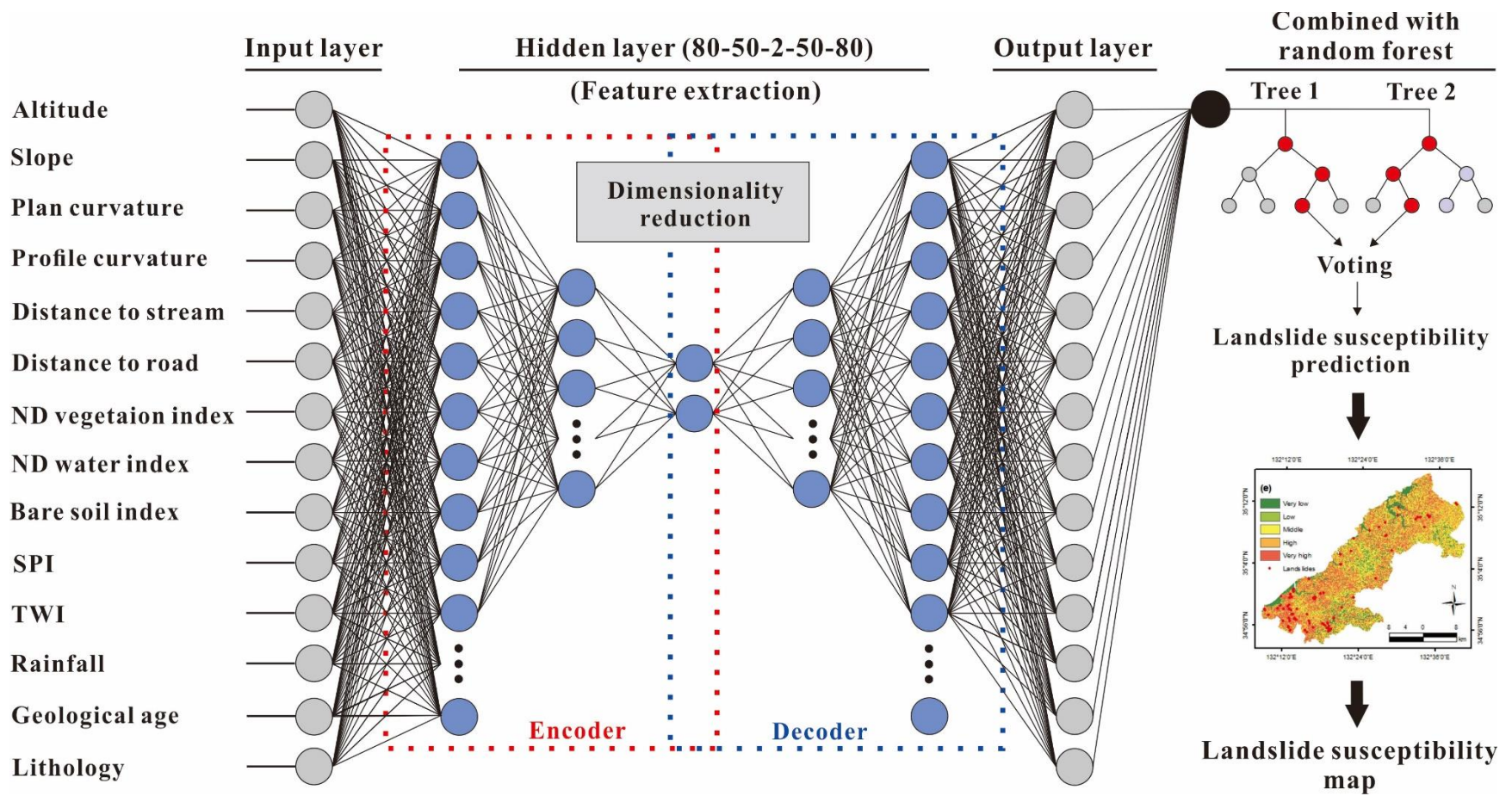
Fig. 4.7 Architecture of random forest combined with stacked autoencoder employing reconstruction error value by anomaly detection
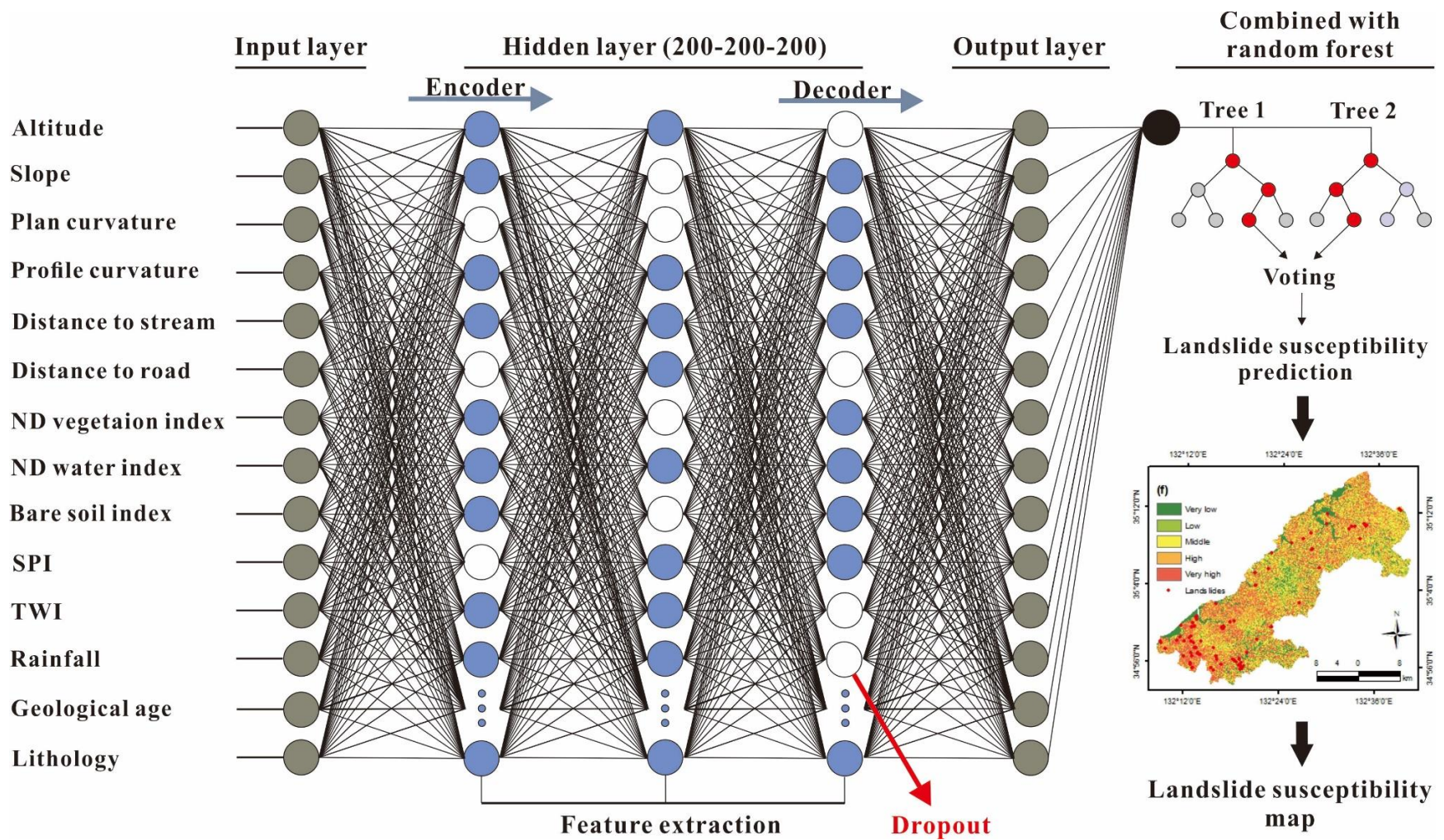
Fig. 4.8 Architecture of random forest combined with sparse autoencoder employing reconstruction error value by anomaly detection
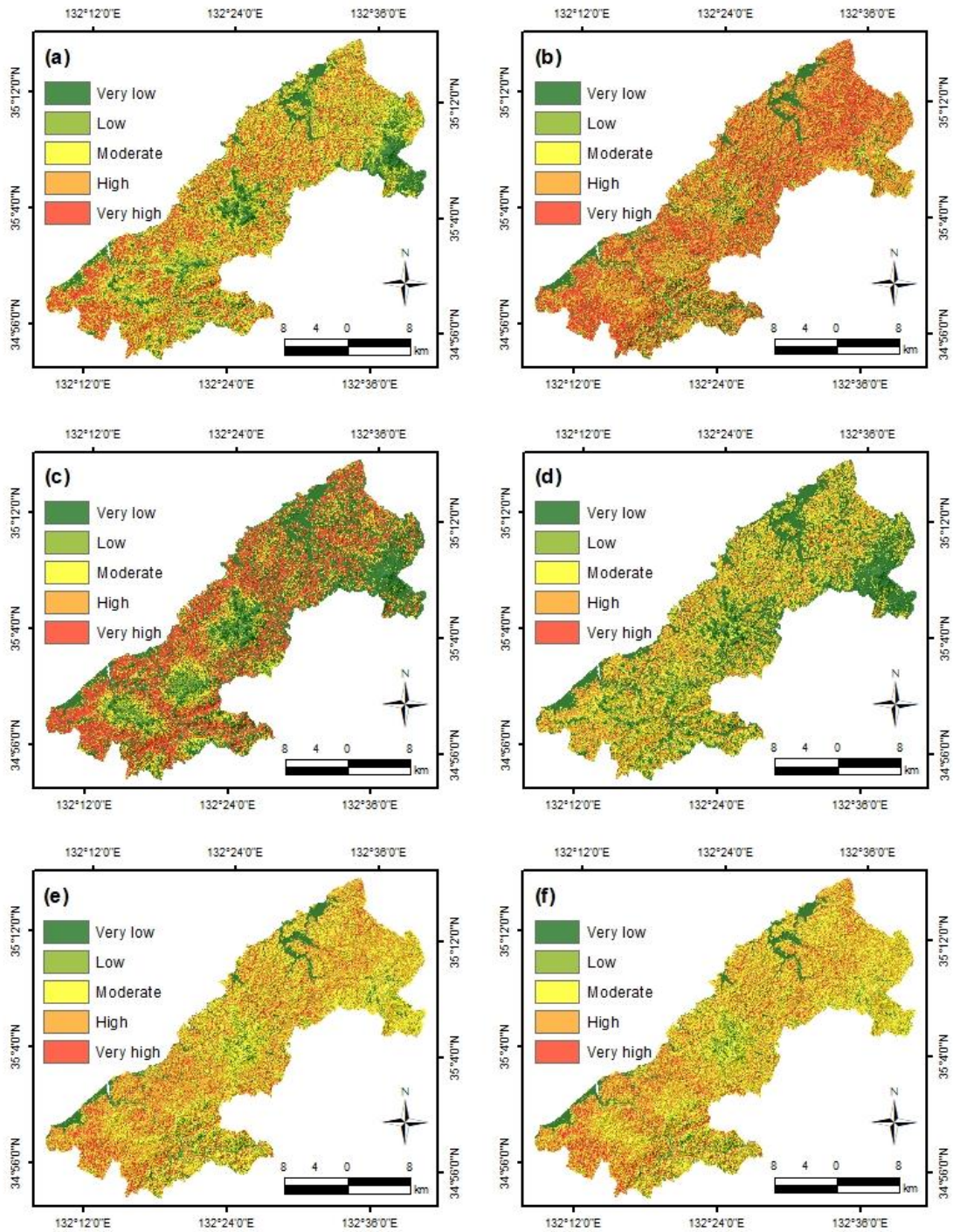
Fig. 4.9 Landslide susceptibility maps of Shimane Prefecture using (a) Support vector machine, (b) Random forest, (c) Stacked autoencoder, (d) Sparse autoencoder, (e) Stacked autoencoder combined with RF, (f) Sparse autoencoder combined with RF

4.2.2 Validation on landslide susceptibility prediction in Shimane Prefecture

The landslide susceptibility assessment was verified using the area under the curve on the validation dataset for six model. The predictive ratio for landslide susceptibility assessment are mainly calculated by confusion matrix. The true positive rate (TPR) defined as the ratio of true positive to the sum of true positive and false negative, the false positive rate (FPR) defined as the ratio of false positive to the sum of false positive and true negative to the number of validation samples (Chen et al. 2018a; Zhang and Wang, 2019). In general, the true positive defines the landslide grid cells that are predictive as landslides, true negative means non-landslide grid cells that are predictive as non-landslides, false-positive reflects non-landslide grid cells that are predictive as landslides, and false negative means landslide grid cells that are predictive as non-landslides (Huang et al. 2019). The area under the curve was applied to assess the prediction performance of landslide susceptibility index values on the validation dataset. The prediction rate values of SVM, RF, StAE, SpAE, StAE with RF and SpAE with RF model are obtained by calculating the area under the prediction rate curves. The StAE with RF and SpAE model of combined classifier have relatively higher prediction rates than using SVM, RF, StAE, and SpAE model of single classifier (Fig. 4.10). It means that the classifiers combined with both autoencoder and traditional machine learning are better than using a single classifier.

Table 4.4 Number of landslides and percent of landslide susceptibility class area

Landslide susceptibility class (index value)	SVM		RF		StAE		SpAE		StAE with RF		SpAE with RF	
	No.	%	No.	%	No.	%	No.	%	No.	%	No.	%
Very low (0 - 0.2)	15	17.00	1	11.80	5	35.65	7	30.16	2	6.31	3	5.82
Low (0.2 - 0.4)	4	19.61	2	10.45	1	11.09	10	19.07	6	13.58	8	14.38
Moderate (0.4 - 0.6)	7	25.83	4	8.43	3	10.52	15	24.73	16	33.04	13	35.96
High (0.6 - 0.8)	17	24.94	13	33.43	4	13.07	44	22.60	66	36.81	66	33.25
Very high (0.8 - 1.0)	47	12.62	70	35.89	77	29.67	14	3.44	0	10.26	0	10.59
Sum	90	100	90	100	90	100	90	100	90	100	90	100
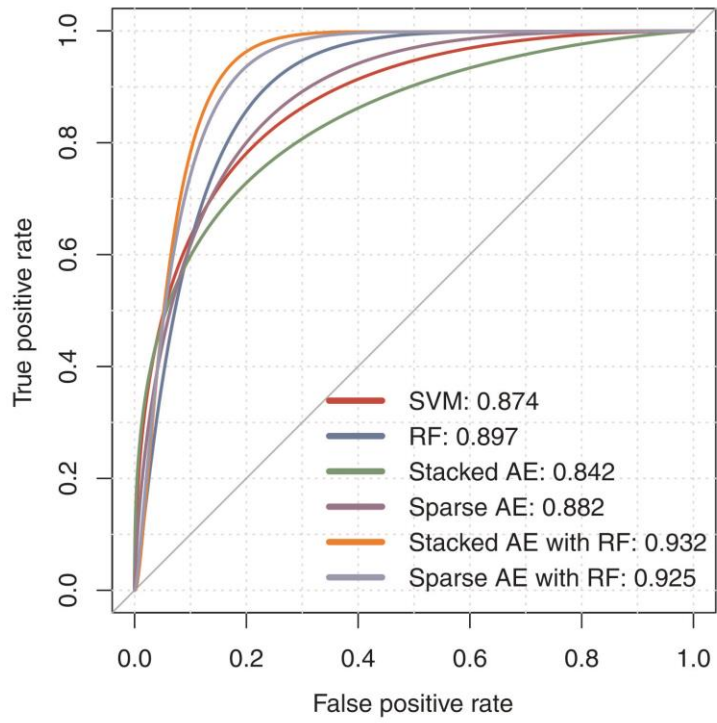
Fig. 4.10 The area under the curves for prediction ratio and validation of landslide susceptibility maps by the six models

Conclusions

This study investigated the application of an autoencoder framework, and autoencoder combined with machine learning for landslide susceptibility assessment and prediction in Iburi region, Hokkaido and Oda City and Gotsu City, Shimane Prefecture.

As a case study for landslides triggered by earthquake, Iburi region of Hokkaido in Northern Japan are selected by applying 12 sampling strategies to landslide susceptibility mapping. The validation of the results was conducted based on the objective measures of the area under the curve in precision and recall, TPR and TNR, TPR and FPR, and accuracy. The experimental results led to the following conclusions.

1. Various sampling strategies showed improved accuracy in landslide susceptibility assessment, which should be analyzed and compare with precision and recall curve in imbalanced data.
2. The prediction results obtained using the proposed autoencoder framework had good performance in terms of the area under the curve in precision and recall, TPR and TNR, TPR and FPR, and accuracy.
3. For the various models, the best performance by means of confusion matrix, especially in areas where landslides were triggered by the earthquake, was to utilize a sampling ratio of 1:2 of landslides and non-landslides generated in the PM.

Finally, the prediction accuracies of landslide susceptibility mapping using the autoencoder model can be effectively improved by two strategies: 1) hyperparameter tuning in constructing the autoencoder architecture; 2) the selection of the tanh activation function. The landslide susceptibility maps produced in this study could be useful for decision-makers, planners, and engineers in disaster planning to mitigate economic losses and casualties. In future research, the accuracy of the landslide susceptibility maps in this study could be enhanced by selecting the optimal sampling strategy and investigating highly efficient deep learning techniques.

For case study of landslides triggered by extreme rainfall, the landslides in Oda City and Gotsu City in Shimane Prefecture, southwestern Japan are used. In this study, the classifiers combined with both deep learning and traditional machine learning, StAE with RF and SpAE with RF models, are proposed for landslide susceptibility prediction. The autoencoder consists of input layers for raw data, hidden layers for feature extraction, and output layers for landslide susceptibility prediction. Several impressive characteristics were revealed in landslide susceptibility assessment in the Oda City and Gotsu City in Shimane Prefecture:

1. The combined classifiers have the advantage of both machine learning and deep learning, i.e., dimension reduction of the StAE model and dropout of the SpAE model for feature extraction.
2. The correlation between landslides and landslide affecting factors using frequency ratio was high in NDVI, distance to road, and altitude.
3. Performance assessment was carried out with the SVM, RF, StAE, SpAE, StAE with RF, and SpAE with RF models. The results show that the proposed StAE with RF and SpAE with RF models have a relatively better prediction rate than a single classifier such as SVM, RF, StAE and SpAE models.

In conclusion, the proposed combined classifier is promising for classification between landslide and non-landslide following landslide susceptibility prediction because it can overcome the limitations of conventional machine learning algorithms, extract features and pattern recognition, reduce computations, and improve performance.

References

Aditian A, Kubota T, Shinohara Y (2018) Comparison of GIS-based landslide susceptibility models using frequency ratio, logistic regression, and artificial neural network in a tertiary region of Ambon, Indonesia. Geomorphology 318:101-111.

Alessandro T, Carla I, Carlo E, Gabriele SM (2015) Comparison of logistic regression and random forests techniques for shallow landslide susceptibility assessment in Giampilieri (NE Sicily, Italy). Geomorphology 249:119-136.

Alexakis D, Agapiou A, Tzouvaras M, Themistocleous K, Neocleous K, Michaelides S, Hadjimitsis D (2014) Integrated use of GIS and remote sensing for monitoring landslides in transportation pavements: the case study of Paphos area in Cyprus. Natural Hazards 72:119-141.

Althuwaynee OF, Pradhan B, Lee S (2016) A novel integrated model for assessing landslide susceptibility mapping using CHAID and AHP pair-wise comparison. International Journal of Remote Sensing 37(5):1190-1209.

Arnone E, Francipane A, Scarbaci A, Puglisi C, Noto LV (2016) Effect of raster resolution and polygon-conversion algorithm on landslide susceptibility mapping. Environmental Modelling and Software 84:467-481.

Ayalew L, Yamagishi H (2005) The application of GIS-based logistic regression for landslide susceptibility mapping in the Kakuda-Yahiko Mountains, Central Japan. Geomorphology 65:15-31.

Ayinde BO, Inanc T, Zurada JM (2019) Regularizing deep neural networks by enhancing diversity in feature extraction. IEEE Transactions on Neural Networks and Learning Systems 30(9):1-12.

Bai S, Wang J, Lü G, Zhou P, Hou S, Xu S (2010) GIS-based logistic regression for landslide susceptibility mapping of the Zhongxian segment in the Three Gorges area, China. Geomorphology 115:23-31.

Ballabio C, Sterlacchini S (2012) Support vector machines for landslide susceptibility mapping: the Staffora River Basin case study, Italy. Mathematical Geosciences 44(1):47-70.

Borrelli L, Ciurleo M, Gullà G (2018) Shallow landslide susceptibility assessment in granitic rocks using GIS-based statistical methods: the contribution of the weathering grade map. Landslides 15(6):1127-1142.

Charte D, Charte F, García S, Jesus MJ, Herrera F (2018) A practical tutorial on autoencoders for nonlinear feature fusion: taxonomy, models, software and guidelines. Information Fusion 44:78-96.

Chen H, Zeng Z, Tang H (2015) Landslide deformation prediction based on recurrent neural network. Neural Processing Letters 41(2):169-178.

Chen W, Panahi M, Tsangaratos P, Shahabi H, Ilia I, Panahi S, Li S, Jaafari A, Ahmadg BB (2019a) Applying population-based evolutionary algorithms and a neuro-fuzzy system for modeling landslide susceptibility. Catena 172:212-231.

Chen W, Peng J, Hong H, Shahabi H, Pradhan B, Liu J, Zhu AX, Pei X, Duan Z (2018a) Landslide susceptibility modelling using GIS-based machine learning techniques for Chongren county, Jiangxi province, China. Science of The Total Environment 626:1121-1135.

Chen W, Sun Z, Han J (2019b) Landslide susceptibility modeling using integrated ensemble weights of evidence with logistic regression and random forest models. Applied Science 9(1):171.

Chen W, Zhang S, Li R, Shahabi H (2018b) Performance evaluation of the GIS-based data mining techniques of best-first decision tree, random forest, and naïve Bayes tree for landslide susceptibility modeling. Science of The Total Environment 644:1006-1018.

Ciampalini A, Raspini F, Bianchini S, Frodella W, Bardi F, Lagomarsino D, Traglia F, Moretti S, Proietti C, Pagliara P, Onori R, Corazza A, Duro A, Basile G, Casagli N (2015) Remote sensing as tool for development of landslide databases: the case of the Messina Province (Italy) geodatabase. Geomorphology 249:103-118.

Colkesen I, Sahin EK, Kavzoglu T (2016) Susceptibility mapping of shallow landslides using kernel-based Gaussian process, support vector machines and logistic regression. Journal of African Earth Sciences 118:53-64.

Corominas, J, Van Westen C, Frattini P, Cascini L, Malet J, Fotopoulou S, Catani F, Van Den Eeckhaut M, Mavrouli O, Agliardi F, Pitilakis K, Winter M, Pastor M, Ferlisi S, Tofani V, Hervás J, Smith J (2013) Recommendations for the quantitative analysis of landslide risk. Bulletin of Engineering Geology and the Environment 73(2):209-263.

Dagdelenler G, Nefeslioglu HA, Gokceoglu C (2016) Modification of seed cell sampling strategy for landslide susceptibility mapping: an application from the eastern part of the Gallipoli peninsula (Canakkale, Turkey). Bulletin of Engineering Geology and the Environment 75(2):575-590.

Devkota KC, Regmi AD, Pourghasemi HR, Yoshida K, Pradhan B, Ryu IC, Dhital MR, Althuwaynee OF (2013) Landslide susceptibility mapping using certainty factor, index of entropy and logistic regression models in GIS and their comparison at Mugling-Narayanghat road section in Nepal Himalaya. Natural Hazards 65(1):135-165.

Di Martire D, Tessitore S, Brancato D, Ciminelli MG, Costabile S, Costantini M, Graziano GV, Minati F, Ramondini M, Calcaterra D (2016) Landslide detection integrated system (LaDIS) based on in-situ and satellite SAR interferometry measurements. Catena 137:406-421.

Fell R, Corominas J, Bonnard C, Cascini L, Leroi E, Savage W (2008) Guidelines for landslide susceptibility, hazard and risk zoning for land use planning. Engineering Geology 102(3-4): 85-98.

Fujiwara S, Nakano T, Morishita Y, Kobayashi T, Yarai H, Une H, Hayashi K (2019) Detection and interpretation of local surface deformation from the 2018 Hokkaido Eastern Iburi Earthquake using ALOS-2 SAR data. Earth, Planets and Space 71:64.

Gedeon TD (1997) Data mining of inputs: analyzing magnitude and functional measures. International Journal of Neural Systems 8(2):209-18.

Goetz JN, Brenning A, Petschko H, Leopold P (2015) Evaluating machine learning and statistical prediction techniques for landslide susceptibility modeling. Computers & Geosciences 81:1-11.

Guo C, David RM, Zhang Y, Wang K, Yang Z (2015) Quantitative assessment of landslide susceptibility along the Xianshuihe fault zone, Tibetan Plateau, China. Geomorphology 248:93-110.

Heckmann T, Gegg K, Gegg A, Becht M (2014) Sample size matters: investigating the effect of sample size on a logistic regression susceptibility model for debris flows. Natural Hazards and Earth System Sciences 14:259-278.

Hinton GE, Salakhutdinov RR (2006) Reducing the dimensionality of data with neural networks. Science 313:504-507.

Hong H, Ilia I, Tsangaratos P, Chen W, Xu C (2017) A hybrid fuzzy weight of evidence method in landslide susceptibility analysis on the Wuyuan Area, China. Geomorphology 290:1-16.

Hong H, Pourghasemi HR, Pourtaghi ZS (2016) Landslide susceptibility assessment in Lianhua County (China): a comparison between a random forest data mining technique and bivariate and multivariate statistical models. Geomorphology 259:105-118.

Hua Y, Zhao D, Xu Y, Wang Z (2019) Arc-arc collision caused the 2018 Eastern Iburi earthquake (M 6.7) in Hokkaido, Japan. Nature 9(13914)

Huang F, Zhang J, Zhou C, Wang Y, Huang J, Zhu L (2019) A deep learning algorithm using a fully connected sparse autoencoder neural network for landslide susceptibility prediction. Landslides 1-13.

Huang L, Xiang LY (2018) Method for meteorological early warning of precipitation-induced landslides based on deep neural network. Neural Processing Letters 48(2):1243-1260.

Huang Y, Zhao L (2018) Review on landslide susceptibility mapping using support vector machines. Catena 165:520-529.

Kameda J, Kamiya H, Masumoto H, Morisaki T, Hiratsuka T, Inaoi C, (2019) Fluidized landslides triggered by the liquefaction of subsurface volcanic deposits during the 2018 Iburi–Tobu earthquake, Hokkaido, Nature 9(13119)

Kimura G (1994) The latest Cretaceous-early Paleogene rapid growth of accretionary complex and exhumation of high pressure series metamorphic rocks in Northwestern Pacific margin. Journal of Geophysical Research Solid Earth 99(B11):22147-22164.

King G, Zeng L (2001) Logistic regression in rare events data. Political Analysis 9:137-163.

Kuritani T, Nakagawa M, (2016) Origin of ultra rear-arc magmatism at Rishiri Volcano, Kuril Arc. Geochemistry, Geophysics, Geosystems 17(2):4032-4050

LeCun Y, Bengio Y, Hinton G (2015) Deep learning. Nature 521:436.

Lee S, Talib JA (2005) Probabilistic landslide susceptibility and factor effect analysis. Environmental Geology 47(7):982-990.

Lin GF, Chang MJ, Huang YC, Ho JY (2017) Assessment of susceptibility to rainfall induced landslides using improved self-organizing linear output map, support vector machine, and logistic regression. Engineering Geology 224:62-74.

Liu Y, Wu L (2016) Geological disaster recognition on optical remote sensing images using deep learning. Procedia Computer Science 91:566-575.

Luo X, Lin F, Zhu S, Yu M, Zhang Z, Meng L, Peng J (2019) Mine landslide susceptibility assessment using IVM, ANN and SVM models considering the contribution of affecting factors. Public Library of Science 14(4):1-18.

Lu P, Qin Y, Li Z, Mondini AC, Casagli N (2019) Landslide mapping from multi-sensor data through improved change detection-based Markov random field. Remote Sensing of Environment 231:1-17.

Mabu S, Fujita K, Kuremoto T (2019) Disaster area detection from synthetic aperture radar images using convolutional autoencoder and one-class SVM. Journal of Robotics, Networking and Artificial Life 6(1): 48-51.

Melchiorre C, Matteucci M, Azzoni A, Zanchi A (2008) Artificial neural networks and cluster analysis in landslide susceptibility zonation. Geomorphology 94(3-4):379-400.

Meten M, Prakash B, Yatabe R (2015) Effect of landslide factor combinations on the prediction accuracy of landslide susceptibility maps in the Blue Nile gorge of Central Ethiopia. Geoenvironmental Disasters 2:1-17.

Meusburger K, Alewell C (2009) On the influence of temporal change on the validity of landslide susceptibility maps. Natural Hazards and Earth System Sciences 9:1495-1507.

Ng A (2011) Sparse autoencoder. CS294A Lecture notes 72.

Park I, Choi J, Lee M, Lee S (2012) Application of an adaptive neuro-fuzzy inference system to ground subsidence hazard mapping. Computers and Geosciences 48:228-238.

Park S, Hamm S, Kim J (2019) Performance evaluation of the GIS-based data-mining techniques decision tree, random forest, and rotation forest for landslide susceptibility modeling. Sustainability 11(20):5659.

Park S, Kim J (2019) Landslide susceptibility mapping based on random forest and boosted regression tree models, and a comparison of their performance. Applied Science 9(5):942.

Pradhan B, Lee S, Buchroithner MF (2010) GIS-based back-propagation neural network model and its cross-application and validation for landslide susceptibility analyses. Computers, Environment and Urban Systems 34:216-235.

Raja NB, Cicek I, Turkoglu N, Aydin O, Kawasaki A (2017) Landslide susceptibility mapping of the Sera River Basin using logistic regression model. Natural Hazards 85:1323-1346.

Romero A, Gatta C, Camps-Valls G (2016) Unsupervised deep feature extraction for remote sensing image classification. IEEE Transactions on Geoscience and Remote Sensing 54(3):1349-1362.

Roy J, Saha S (2019) Landslide susceptibility mapping using knowledge driven statistical models in Darjeeling District, West Bengal, India. Geoenvironmental Disasters 6:1-18.

Saito H, Nakayama D, Matsuyama H (2009) Comparison of landslide susceptibility based on a decision-tree model and actual landslide occurrence: the Akaishi Mountains, Japan. Geomorphology 109(3):108-121.

Segoni S, Tofani V, Rosi A, Catani F, Casagli N (2018) Combination of rainfall thresholds and susceptibility maps for dynamic landslide hazard assessment at regional scale. Frontiers in Earth Science 6(85):1-11.

Scornet E (2016) Learning with random forests. Thesis in Pierre and Marie Curie University.

Shin J (2015) A study on stacked autoencoders and its fine-tuning. Thesis in Seoul National University.

Tajika J, Ohtsu S, Inui T (2016) Interior structure and sliding process of landslide body composed of stratified pyroclastic fall deposits at the Apporo 1 archaeological site, southeastern margin of the Ishikari Lowland, Hokkaido, Northern Japan. The Journal of the Geological Society of Japan 122(1):23-35.

Tamaki M, Kusumoto S, Itoh Y (2010) Formation and deformation processes of late Paleogene sedimentary basins in southern central Hokkaido, Japan: paleomagnetic and numerical modeling approach. Island Arc 19(2):243-258.

Tien Bui D, Pradhan B, Lofman O, Revhaug I (2012) Landslide susceptibility assessment in Vietnam using support vector machines, decision tree, and Naïve Bayes models. Mathematical Problems in Engineering 2012:1-26.

Tien Bui D, Ho TC, Pradhan B, Pham BT, Nhu VH, Revhaug I (2016) GIS-based modeling of rainfall-induced landslides using data mining-based functional trees classifier with AdaBoost, Bagging, and MultiBoost ensemble frameworks. Environmental Earth Sciences 75:1-22.

Trigila A, Iadanza C, Esposito C, Scarascia-Mugnozza G (2015) Comparison of logistic regression and random forests techniques for shallow landslide susceptibility assessment in Giampilieri (NE Sicily, Italy). Geomorphology 249(15):119-136.

Tsangaratos P, Ilia I (2016) Comparison of a logistic regression and naïve Bayes classifier in landslide susceptibility assessments: The influence of models complexity and training dataset size. Catena 145:164-179.

Tsangaratos P, Ilia I, Hong H, Chen W, Xu C (2017) Applying information theory and GIS-based quantitative methods to produce landslide susceptibility maps in Nancheng County, China. Landslides 14(3):1091-1111.

Van Den Eeckhaut M, Marre A, Poesen J (2010) Comparison of two landslide susceptibility assessments in the Champagne-Ardenne region (France). Geomorphology 115(1-2):41-155.

Wang Y, Fang Z, Hong H (2019) Comparison of convolutional neural networks for landslide susceptibility mapping in Yanshan County, China. Science of the Total Environment 666:975-993.

Westen CJV, Rengers N, Soeters R (2003) Use of geomorphological information in indirect landslide susceptibility assessment. Natural Hazards 30(3):399-419.

Xiao L, Zhang Y, Peng G (2018) Landslide susceptibility assessment using integrated deep learning algorithm along the China-Nepal highway. Sensors 18:1-13.

Xu C, Dai F, Xu X, Lee YH (2012) GIS-based support vector machine modeling of earthquake-triggered landslide susceptibility in the Jianjiang River watershed, China. Geomorphology 145-146:70-80.

Yalcin A (2008) GIS-based landslide susceptibility mapping using analytical hierarchy process and bivariate statistics in Ardesen (Turkey): comparisons of results and confirmations. Catena 72:1-12.

Yang BB, Yin KL, Lacasse S, Liu ZQ (2019) Time series analysis and long short-term memory neural network to predict landslide displacement. Landslides 16(4):677-694.

Yao X, Tham LG, Dai FC (2008) Landslide susceptibility mapping based on support vector machine: a case study on natural slopes of Hong Kong, China. Geomorphology 101:572-582.

Yeon Y, Han J, Ryu K (2010) Landslide susceptibility mapping in Injae, Korea, using a decision tree. Engineering Geology 116:274-283.

Yilmaz C, Topal T, Süzen ML (2012) GIS-based landslide susceptibility mapping using bivariate statistical analysis in Devrek (Zonguldak-Turkey). Environmental Earth Sciences 65(7):2161-2178.

Yilmaz I (2010) Comparison of landslide susceptibility mapping methodologies for Koyulhisar, Turkey: conditional probability, logistic regression, artificial neural networks, and support vector machine. Environmental Earth Sciences 61:821-836.

Yu S, Príncipe JC (2019) Understanding autoencoders with information theoretic concepts. Neural Networks 117:104-123.

Zhang S, Li R, Wang FW, Iio A (2019) Characteristics of landslides triggered by the 2018 Hokkaido Eastern Iburi earthquake, Northern Japan. Landslides 16(9):1691-1708.

Zhang S, Wang FW (2019) Three-dimensional seismic slope stability assessment with the application of Scoops3D and GIS: a case study in Atsuma, Hokkaido. Geoenvironmental Disasters 6:1-14.

Zhang R, Isola P, Efros AA (2017) Split-brain autoencoders: unsupervised learning by cross-channel prediction. Paper presented at the Computer Vision & Pattern Recognition.

Zhou S, Fang L (2015) Support vector machine modeling of earthquake-induced landslides susceptibility in central part of Sichuan province, China. Geoenvironmental Disasters 2:1-12.

Zhu X, Miao Y, Yang L, Bai S, Liu J, Hong H (2018) Comparison of the presence-only method and presence-absence method in landslide susceptibility mapping. Catena 171:222-233.